

SiO Maser Survey of the Large-Amplitude Variables in the Galactic Center

Shuji DEGUCHI¹, Hiroshi IMAI^{2,3,4}, Takahiro FUJII^{2,4}, Ian S. GLASS⁵, Yoshifusa ITA⁶, Hideyuki IZUMIURA⁷, Osamu KAMEYA^{2,8}, Atsushi MIYAZAKI¹, Yoshikazu NAKADA⁶

and

Jun-ichi NAKASHIMA^{9,10}

¹ Nobeyama Radio Observatory, National Astronomical Observatory, Minamimaki, Minamisaku, Nagano 384-1305

² VERA Project Office, National Astronomical Observatory, 2-21-1 Osawa, Mitaka, Tokyo 181-8588

³ Joint Institute for VLBI in Europe, Postbus 2, 7990 AA Dwingeloo, The Netherlands

⁴ Faculty of Science, Kagoshima University, 1-21-35 Korimoto, Kagoshima 890-0065

⁵ South African Astronomical Observatory, PO Box 9, Observatory 7935, South Africa

⁶ Institute of Astronomy, School of Science, The University of Tokyo, 2-21-1 Osawa, Mitaka, Tokyo 181-0015

⁷ Okayama Astrophysical Observatory, National Astronomical Observatory, Kamogata, Asakuchi, Okayama 719-0232

⁸ Mizusawa Astrodynamics Observatory, National Astronomical Observatory, Mizusawa, Iwate 023-0861

⁹ Department of Astronomical Science, The Graduate University for Advanced Studies, Minamimaki, Minamisaku, Nagano 384-1305

¹⁰ Department of Astronomy, University of Illinois at Urbana-Champaign, 1002 W. Green St., Urbana, IL 61801-3074, U.S.A.

(PASJ April 28 issue in press— Version: 2004/02/27)

(Received 2003 October 22; accepted 2003 0)

Abstract

We have surveyed ~ 400 known large-amplitude variables within $15'$ of the galactic center in the SiO $J = 1-0$ $v = 1$ and 2 maser lines at 43 GHz, resulting in 180 detections. SiO lines were also detected from 16 other sources, which are located within $20''$ (the telescope half beamwidth) of the program objects. The detection rate of 48 percent is comparable to that obtained in Bulge IRAS source surveys. Among the SiO detections, five stars have radial velocities greater than 200 km s^{-1} . The SiO detection rate increases steeply with the period of light variation, particularly for stars with $P > 500$ d, where it exceeds 80%. We found that, at a given period, the SiO detection rate is approximately three times that for OH. These facts suggest

that the large-amplitude variables in the Nuclear Disk region are AGB stars similar in their overall properties to the inner and outer Bulge IRAS/SiO sources. From the set of radial velocity data, the mass distribution within 30 pc of the galactic center is derived by a new method which is based on the collisionless Boltzmann equation integrated along the line of sight. The mass within 30 pc is about $6.4[\pm 0.7] \times 10^7 M_{\odot}$ and the mass of the central black hole is $2.7[\pm 1.3] \times 10^6 M_{\odot}$. Consideration of the line-of-sight velocity of each star and its potential energy leads to the conclusion that the five high-velocity stars come from galactocentric distances as high as 300 pc. The high-velocity subsample of stars with negative radial velocities exhibits a tendency to have brighter K magnitudes than the subsample of stars with positive velocities. The origin of these high-velocity stars is discussed.

Key words: Galaxy: center, kinematics and dynamics — masers — stars: AGB and post-AGB

1. Introduction

Radial-velocity data concerning stellar maser sources are useful for studying the dynamical behavior of the central part of the Galaxy (Lindqvist et al. 1992; Izumiura et al. 1995; Sjouwerman et al. 1998; Deguchi et al. 2000). At visible wavelengths, they are difficult to obtain in the galactic center region because of interstellar extinction. Instead, most information comes from radio or near-infrared observations [for example, Sellgren et al. (1987)]. In particular, observations of SiO and OH masers give radial velocities of stars accurate to within a few km s^{-1} . The masers arise in the circumstellar envelopes of mass-losing stars on the Asymptotic Giant Branch (AGB), which are intrinsically bright in the near- and mid-infrared regions, and which can potentially be identified at these wavelengths. Large numbers of candidate stars suitable for pointed maser surveys toward the nuclear disk have been discovered in the near-infrared K band by making use of their characteristic large-amplitude variability (Glass et al. 2001).

The dynamical behavior of the central region of the Galaxy has attracted much attention, especially in relation to the central black hole (for example, Morris, Serabyn 1996). Proper motions of stars have been measured in the near-infrared K band near the black hole (Genzel et al. 2000; Ghez et al. 2000), and proper motions of SiO maser stars have also been measured within the central $15''$ (Reid et al. 2003). These were used to find the position of Sgr A* in the K -band images (Menten et al. 1997). This paper concentrates on the dynamics of stars located towards the outer part of the central star cluster around the black hole, i.e., at about 2–30 pc distance, where the gravitational force of the black hole ceases to influence the stellar motions, and the stellar system is nearly self-gravitating. The dynamical (rotational) time scale in this region is a few $\times 10^6$ y, while the ages of the AGB stars are $10^7 - 10^9$ y. Therefore,

these stars are considered to be dynamically well relaxed (e.g., Hozumi et al. 2000). Since the bar-like structure of the Galactic bulge was discovered (Blitz, Spergel 1991; Nakada et al. 1991; Dwek et al. 1995), it has been recognized that non-circular motions must be taken into account when interpreting observational data such as the CO gas distribution in the central nuclear disk (Binney et al. 1991; Weiner, Sellwood 1999). Because double bars and nuclear rings have been proposed as efficient mechanisms for feeding gas into the centers of galaxies (Shlosman et al. 1989), it has become additionally important to look for signs of non-circularity in the motions of gas and stars.

In this paper, we report on the results of an SiO maser survey of Large Amplitude Variables (Miras or semiregulars; abbreviated as LAV hereafter) in a $24' \times 24'$ area of the galactic center (Glass et al. 2001), whose amplitudes and periods are known (Wood et al. 1998; Glass et al. 2001). Because these stars are located at approximately the same distance (about 8 kpc) from the Sun, they constitute an ideal sample for studying the statistical characteristics of AGB stars and their detectability in the maser lines. In addition, surveying these sources gives accurate radial velocities, and provides basic data for investigating the kinematics of the galactic nuclear disk. Although the mass within this region has been obtained previously by various methods [for example, Lindqvist et al. (1992)], none of them [except Saha et al. (1996)] are fully valid for treating the problem; the results obtained are likely to be in error by a factor of a few between the radii of 2 and 30pc. In this paper, we analyze the new SiO radial-velocity data set using the Boltzmann equation integrated along the line of sight. We also consider the origin of the high-velocity stars seen toward the galactic center.

2. Observations

Simultaneous observations in the SiO $J = 1-0$, $v = 1$ and 2 transitions at 42.122 and 42.821 GHz, respectively, were made with the 45-m radio telescope at Nobeyama during the periods of 2001 February–May, 2002 March–May, and 2003 May. We used a cooled SIS mixer receiver (S40) for the 43 GHz observations and acousto-optical spectrometer arrays, AOS-H and AOS-W, having bandwidths of 40 and 250 MHz. The effective velocity resolution of the AOS-H spectrometer is 0.3 km s^{-1} . They cover the velocity range of $\pm 350 \text{ km s}^{-1}$, for both the SiO $J = 1-0$ $v = 1$ and 2 transitions, simultaneously. The overall system temperature was between 200 and 300 K, depending on the weather condition. The half-power telescope beam width (HPBW) is about $40''$. The antenna temperature (T_a) given in the present paper is that corrected for the atmospheric and telescope ohmic loss but not for the beam or aperture efficiency. The conversion factor of the antenna temperature to the flux density is about 2.9 Jy K^{-1} . To save observation time, we employed the position switching sequence, Off–On1–On2–On3, where the off position was taken 7 arc minutes west of the first-object position (On1) in right ascension; the separation of the off position corresponds to the angle moved by an object in the sky during the typical integration (20 s), additional telescope-slewing, and settling time (10

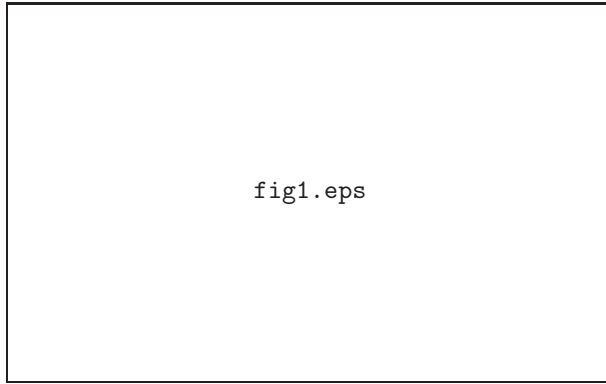


Fig. 1. Source distribution in the galactic coordinates. Filled and unfilled circles indicate the SiO detections and nondetections.

s), so that the integrations were made at nearly the same elevation angle. With this sequence, we observed three stars at once and saved about 50% of the total observation time. Further details of SiO maser observations using the NRO 45-m telescope have been described elsewhere (Deguchi et al. 2000), and are not repeated here.

The sources observed in this paper are the large-amplitude variables (LAVs) in a $24' \times 24'$ area of the galactic center (Glass et al. 2001). The positions of the observed sources are shown in Figure 1. In this sample, the star name was designated by field and object numbers, e.g., 3–49. The total number of the objects listed in Glass et al. (2001) was 418. Note that, however, a star near the edge of a field was sometimes given a second name because it appeared in an adjacent field. We counted 15 such objects; the measured positions of these stars are coincident with a few arcsec accuracy. In field 11, the positions turned out to be shifted by about $30''$ and corrected values were listed in an erratum (Glass et al. 2001); note that the latter includes an additional variable, 11-307. Additionally, three LAV stars, which were identified later with the help of ISOGAL observations (Omont et al. 2003), were observed. The positions of these 3 stars are given in table 1.

In summary, we observed 396 LAVs over three years. The SiO detections and nondetections are summarized in tables 2 and 3, respectively. The spectra of the SiO detections are shown in Figure 2a–2k. In the Glass et al. (2001)'s list, some objects are located very close to each other and they fall within one beam diameter of the 45-m telescope ($40''$). We observed only one object of each such close pair, because they are unresolvable in our beam. We list such objects lying closer than $12''$ from each other in table 4, together with those that have more than one name assignment in the LAV survey. The objects in table 4 were thus considered to have been observed. In the final accounting of such overlapped observations etc., in 2003, two sources were found to be still missing; 4–22 and 11–307 (which was added in the erratum) was not observed. Therefore we made an extra short observation of these two stars in February 2004 together with a previous marginal detection of 4–33. Thus all the LAVs listed by Glass et

al. 2001 have been observed.

Because the surface number density of stars is so high in the galactic center area, we often detected multiple emission peaks in a single beam. When the velocity separation is more than 20 km s^{-1} , they are regarded as different objects. In table 5, we listed such multiple detections in a single beam (of HPBW=40'') and the possible assignment of the sources. The associations with the OH/IR objects (Sjouwerman et al. 1998) are made in terms of the radial velocity (within a few km s^{-1}) and the position (within $\sim 20''$). The identified OH/IR objects were listed in table 6. Furthermore, identifications with previously known SiO/H₂O objects in this area of the sky were also made. These are 1-72, 2-1, 2-18, and 3-266 which are detected in Miyazaki et al. (2001), and 3-5, 3-6, 3-57, 3-88, 3-2885 in Deguchi et al. (2002); 3-3 was detected at 86.7 km/s in 1999 May, but not at this time (2001 April).

When the velocity separation between multiple peaks is less than 20 km s^{-1} , it is impossible to judge whether we are dealing with a single object with multiple peaks, or two close-lying objects within the telescope beam, unless a mapping observation has been made to separate the components. For example, the SiO spectra of 5-157 in Figure 2d show peaks at $V_{\text{lsr}} = -2$ and 6 km s^{-1} . However, we found no significant sources within $30''$ around this object. We tried to separate several multiple-peak objects in the first year (for example, 9-8). However, because of a shortage of observing time in the third year, we were unable to look further into this issue. In table 5, we count 10 cases where source assignments were impossible because of multiple peaks. In our statistics we took the strongest peak to be the given object, for simplicity, and put an asterisk sign after the name.

There is also further confusion in the SiO detections due to time variation. For example, 13-18 (=10-3465) was observed twice in May 2001 and May 2002, but emission was detected at different radial velocities, -16 and 38 km/s . The star 13-4, is located $12.7''$ away from 13-18, but was not detected on May 2003. However, a careful check of the spectra in May 2003 gave weak enhancements of emission at 25 and 40 km/s . We tentatively assign the -16 km s^{-1} component to be 13-18 and discard the May 2002 observations. It is highly possible that the 38 km/s component is 13-4.

Several objects were detected in the off position during the position switching sequence, at $7'$ west of the first-on source (On-1) in right ascension. The off-position detections can easily be recognized; because of the combination of the three objects with one off-position, all of the three spectra have negative emission at the same radial velocity. These are 23-1198 (seen in the spectra of 6-151), and IRAS 17413-2909 (seen in the spectra of 5-27). The -60 km/s component was detected in the spectra of 8-2 and 20-2631 (shown as off-1). This off position was outside of the observed area of Glass et al. (2001), and was named to be SiO359.700+0.079 (17h44m35.9s, $-29^{\circ}09'01''$, J2000); no OH counterpart was found at this position. This position is close to MSX5CG359.6949+00.0742 (17 h44 m36.12s $-29^{\circ}09'27.4''$) with $F_{12}=5.4 \text{ Jy}$. In addition, 24-108 was detected at the off position (in the spectra of 12-6)

in April 2002. We observed this object in May 2003, but the emission was quite weak.

Because of the high chance of contamination by other objects in the telescope beam, the positions and radial velocities of the previously known OH sources were carefully checked to ensure that the cross-identifications are correct. For the sample of both OH and SiO detected objects, the average radial-velocity difference between SiO and OH is $\langle V_{\text{SiO}} - V_{\text{OH}} \rangle = 0.47$ (± 1.88) km s^{-1} , where the standard deviation is shown in the parenthesis. The minimum and maximum of the velocity differences are -3.8 and 4.3 km s^{-1} . These values indicate that the identifications are almost certainly correct and that no large systematic velocity shift occurs between SiO and OH. In terms of OH and SiO velocity differences, an interesting object, 13–200, was found to have an SiO radial velocity at $V_{\text{lrs}}^{\text{SiO}} = 23.7$ km s^{-1} . However, the position of this LAV is close to OH 0.178–0.055 with a separation of $5.1''$, which has $V_{\text{lrs}}^{\text{OH}} = -36.6$ km s^{-1} (Sjouwerman et al. 1998). As noted in Glass et al. (2001), the separation of more than $5''$ is too large to regard as an error in the position measurement. The SiO detection with a large radial velocity difference in this paper proves that these two are surely different stars.

Messineo et al. (2002) surveyed the ISOGAL and MSX sources in the SiO $J = 2-1$ $v = 1$ transition; in their detections, 11 LAVs of Glass et al. (2001) were involved. We checked our detection list and found nine detections (2 negative) in the SiO $J = 1-0$ $v = 1$ and 2 transitions in the present paper. Among their four nondetections of LAVs, we got one detection (20–116) in the present paper. The radial velocities of the SiO $J = 2-1$ $v = 1$ line are coincident with the velocities of the SiO $J = 1-0$ $v = 1$ and 2 transitions within a few km s^{-1} .

Sjouwerman et al. (2002) made targeted surveys for 22 GHz H_2O and 43 GHz SiO maser emission in the galactic center OH/IR stars using the Very Large Array. Only 4 SiO detected objects overlap the LAVs in the present sample, and these are marked † in table 6. Radial velocities also coincide very well with the velocities obtained in this paper. It is curious that none of the objects in the present sample was detected in the H_2O line. In general, the circumstellar H_2O maser line seems to be weak in the LAVs in the galactic center (Taylor et al. 1993; Levine et al. 1995).

3. Discussion

3.1. Period–SiO Detection Rate

In total, 180 LAVs from the original sample were detected in SiO with additional 16 objects. Figure 3 shows the period histogram of all the observed LAVs and the SiO detection rate (line graph with filled circles). The line graph with unfilled circles in figure 3 indicates the OH detection rate, which seems to correlate with the SiO detection rate quite well. Figure 3 clearly shows that the SiO detection rate increases with the period. The maximum detection rate occurs in the 600–700 d period bin. Note that the average period of the Glass et al. (2001) sample is about 430 d. A slight decrease of the detection rate above $P > 700$ d is probably

a statistical effect arising from the small numbers. The same graph was also shown in Imai et al. (2002) for the sample of LAVs with the periods $P > 400$ d and the period measurement quality $Q = 3$ ($Q=3$ the highest quality) preferentially observed in the first year of this program.

In figure 3, we can recognize a small enhancement of the detection rate at the short-period end. There are 16 sources with periods below 200 d; five detections among these are 1–42, 4–28, 6–112, 7–9, and 14–38. The period measurement quality of these LAVs are $Q=2, 0, 1, 3,$ and 3 , where higher Q indicates better measurement quality. Therefore, at least two LAVs of $Q=0$ or 1 are uncertain members of the $P = 100$ – 200 d bin. However, even so, we still have 3 firm detections in this bin. Therefore, we get about a 20% detection rate in this bin after this correction, resulting a relatively flat, but non-zero, detection rate below 300 d. The significant SiO detection rate for periods below 200 d can also be found in the database of stellar maser sources by Benson et al. (1990), though the listed sources are not at the same distances from the Sun. In fact, a significant number of semi-regular variables are known to be involved in the short-period subsample in Benson et al. (1990).

The SiO detection rate is approximately twice (or even triple for certain period ranges) as high as for OH, indicating that the SiO maser survey has doubled the number of stars with radial velocity data near the galactic center. Note, however, that the SiO survey was a targeted survey and OH an unbiased (blind) survey. Therefore, the OH survey (Sjouwerman et al. 1998) detected a number of objects which were not identified in NIR imaging; they are simply not counted in the above comparison of the detection rate between SiO and OH surveys.

That the maser detection rate increases with the period of light variation in LAVs has already been suggested by observations of stars near the Sun (e.g., Benson, Little-Marenin 1996). However, because of uncertainties in the distances of these stars, the relation was not clearly demonstrated. In the present sample, the distances to the LAV stars are almost equal and the correlation with period is much more conclusive.

3.2. Surface density

The surface density distribution of the sample is useful for estimating an approximate line-of-sight distribution of the LAVs. Figure 4 shows plots of the cumulative number of objects, $N(r)$, within a given projected distance from Sgr A*, r , normalized to 1 at the outermost projected distance. The left panel shows the difference between the LAVs and the SiO-detected objects (including all the detections), and the center panel shows the difference between the $l^* > 0$ and $l^* < 0$ SiO detected objects. Here l^* is the longitude offset from Sgr A*. The Kolmogorov-Smirnov test does not give any significant probability of these two sets being statistically different. The distributions can be well approximated by $N(r) \sim r^{1.3}$. This function gives a surface density distribution for SiO or LAV objects that varies as $\sigma(r) \sim r^{-0.7}$. If we assume that the source distribution is spherically symmetric and with a power-law density profile, the number density of the sources (per unit volume) is $\rho(R) \sim R^{-1.7}$, where R is the real

distance from the galactic center (Sgr A*) [see equation (2–43) of Binney & Tremaine (1987)]. The present result fits quite well with the K-band surface density variation near the Center ($\lesssim 6'$), $I_K \sim r^{-0.65}$, measured by Philipp et al. (1999).

In this case, a simple computation gives that, for the sources within a projected distance of $12'$ (~ 30 pc), 32% of the objects are located between the true radii 60 and 300 pc, and 12% of the objects are between the radii 300 and 3 kpc. Furthermore, an integration shows that 31 % of the observed objects in the sample are actually within a radius of 30 pc. The contamination of the sample by SiO objects outside 30 pc is estimated to be as follows; among the ~ 200 SiO detections, 23 objects are outside 300 pc, 112 are sources between 30 and 300 pc, and 65 sources are within 30 pc.

However, the OH 1612 MHz source distribution looks slightly different as shown in the right panel of figure 4 for 137 OH sources within $15.9'$ [taken from Sjouwerman et al. (1998)]. The OH integrated number distribution is approximated by $N_{\text{OH}}(r) \sim r^{0.8}$, leading to a steeper surface density distribution $\sigma(r) \sim r^{-1.2}$, and a number density distribution $\rho(R) \sim R^{-2.2}$. In the right panel, we also plotted the normalized integrated number (thin line) of LAVs with SiO in the present sample (thick dots). The Kolmogorov-Smirnov test gives the probability of 2 % that the two sets have the same statistical distributions. Therefore, we conclude that the distributions *are* different. The integrated number of LAVs with OH in the present sample is also plotted as thin dots (67 objects). As expected, this line falls near the middle of the two sets above. A statistical test does not give any conclusive evidence that the distribution of the LAVs-with-OH set is different from the above two sets (because of small numbers).

The surface density of our LAV sample increases toward the galactic center more slowly than that for OH-sources. This is partly because the near-infrared detection of LAVs is hindered by the high density of stars near the galactic center. In contrast, the OH surveys are less biased near the galactic center. On the other hand, OH detection is enhanced towards the long period end and, hence, toward massive objects [if the masses (luminosities) and periods are correlated as normally assumed]. This fact might imply a mass segregation effect for stars in the galactic center. However, the statistical test for the present SiO sample with OH emission gives a probability of greater than 20 % that the two SiO subsets with and without OH have the same spatial distribution. Therefore, the conjecture of mass segregation cannot be proved by using the present subsample.

Note that the power law obtained for SiO density distribution is close to $R^{-1.75}$. If the mass density of the galactic center area also follows the same rule, the rotational velocity as a function of radius increases as $V(R) \sim R^{0.125}$. Because the $R^{-1.75}$ law makes various physical quantities easy to estimate, we will assume that the density distribution follows this law near the galactic center.

3.3. Velocity Distribution

Figure 5 shows a longitude–velocity diagram for all the SiO detected sources. Here, l^* is the galactic longitude offset from Sgr A* (the dynamical center of the Galaxy; R.A.=18^h45^m40^s.05, Dec.=−29°00′27″.9, J2000; Rogers et al. 1994). Most of the radial velocities fall within ± 200 km s^{−1}. Five extreme sources at $|V_{\text{lsr}}| > 200$ km s^{−1} occupy outlying positions. These sources might be outer bulge objects in highly eccentric orbits, seen by chance in the line of sight toward the galactic center [see discussion in van Langevelde et al. (1992)]. These high-velocity objects appear almost evenly at positive and negative velocities in the present sample. However, they appear only at the negative longitude side of the galactic center ($l^* < 0$).

The regression-line analysis for the radial velocities gives $V_{\text{lsr}} = -6.1(\pm 5.6) + 190.1(\pm 51.2)(l^*/\text{deg})$ km s^{−1} and the standard deviation from this line is 78.0 km s^{−1} for all the 195 sources. If we remove the five extreme sources with $|V_{\text{lsr}}| > 200$ km s^{−1}, the best fit gives $V_{\text{lsr}} = -5.4(\pm 4.5) + 209.8(\pm 41.9)(l^*/\text{deg})$ km s^{−1}. The best-fit slope, 190.1 km s^{−1} per degree, is compatible with the value, ~ 190 km s^{−1} per degree, which was computed from the OH 1612 MHz data within 0.5 degree from the galactic center (Sjouwerman et al. 1998). Considering the slow rotation of the inner Bulge out to 3° of the galactic center, ~ 20 km s^{−1} per degree (Deguchi et al. 2000), we conclude that the nuclear disk is rotating more rapidly than the inner Bulge. The slight shift of the average velocity to the negative side may be interpreted as contamination by foreground objects in stream of stars forming part of a bar-like Bulge (Izumiura et al. 1995; Deguchi et al. 2000).

The overall structure of the SiO l – v diagram is quite similar to the OH l – v diagram in the same region (see figure 3 of Sjouwerman et al. 1998). We can recognize a hole in the SiO distribution at ($l^* = 0.06^\circ$, $V_{\text{lsr}} = 60$ km s^{−1}) in figure 5. The same hole can be seen in figure 3 of Sjouwerman et al. (1998), though another hole at ($l^* = -0.04^\circ$, $V_{\text{lsr}} = -20$ km s^{−1}) in figure 3 of Sjouwerman et al. (1998) does not exist in figure 5. The position of this hole in the l – v diagram corresponds roughly to the dense CO and CS clouds at $V_{\text{lsr}} \sim 75$ km s^{−1}, which can be seen on the overlaid map of figure 5. It is clear that the hole does not simply arise from a bias in the distribution of the LAVs, arising from the near-infrared sampling because it also appears in the unbiased OH survey (Sjouwerman et al. 1998).

Another interesting characteristic of the SiO l – v diagram is no strong association of the SiO radial velocities with the “240 pc molecular-ring” features at $V_{\text{lsr}} \sim -130 - -100$ and $\sim 170 - 190$ km s^{−1}, which can be seen on the overlaid CO map in the left panel of figure 5. This molecular-ring feature is extended in the area of $l = \pm 2^\circ$ and $b = \pm 0.5^\circ$, and is considered to be a manifestation of the bar potential of the Bulge (Binney et al. 1991). On the line of sight toward the galactic center, this ring is located at about 240 pc from the Center itself. A closer look at figure 5 shows that two objects at $V_{\text{lsr}} \sim 170$ km s^{−1} and $l^* = -0.12^\circ$, are on the positive-velocity ring feature, and one is at $V_{\text{lsr}} \sim -140$ km s^{−1} and $l^* = -0.17^\circ$; these are

22–21.2 $[(l, b)=(-0.170, 0.047)]$, 22–21.3, and 22–166 $[(l, b)=(-0.229, 0.044)]$. However, at $b = -0.4^\circ (\sim 2')$, the negative ring feature appears at $V_{\text{lsr}} \sim -75 \text{ km s}^{-1}$ in Oka et al. (1998)’s map. Moreover, the positive-velocity ring feature actually appears very weakly at $V_{\text{lsr}} \sim 165 \text{ km s}^{-1}$ and $l = -0.2^\circ$. The LAVs are therefore not likely to be associated with the ring feature.

It is further reasonable that no parallelogram feature appears in the SiO and OH $l-v$ diagram because the orbits cannot be cusped for the case of stars in a bar-like Bulge (unlike the gas; Binney et al. 1991). Rather, the velocity spread in the SiO $l-v$ diagram is much larger than the velocity spread of the CO gas. These facts indicate that random motions are considerably dominant for stars in this region.

3.4. *The Mass of the Galactic Center*

From the velocity data of maser stars, we can obtain the gravitational mass in the galactic center area in principle. However, this is rather a difficult task because only the line-of-sight velocities and projected distances are known. In the past (Sellgren et al. 1987; Lindqvist et al. 1992), three methods have been used for this purpose: the pressure-balance, projected-mass, and virial methods, where we take the ‘pressure balance method’ to be the moment equation of the Boltzmann equation in the radial direction, as given in Sellgren et al. (1987). Although none of these approaches are really valid for application to the galactic center velocities, we first used them to compute the gravitational masses in order to show that the present sample gives results which are compatible with previous calculations. The results from the pressure-balance and projected-mass methods are presented as filled thin triangles and diamonds in figure 6. For comparison, the previous OH 1612 MHz results (Lindqvist et al. 1992) are also plotted as unfilled thin triangles and diamonds in figure 6.

Because all three of the above noted methods rely on assumptions which are not verified in the case of the galactic center sample in a strict (even rough) sense, they are believed to yield errors of a factor of a few in the computed masses. For example, the pressure balance method uses an equation derived in the radial direction and makes use of line-of-sight quantities.

In order to remedy the situation, we have developed a new method in this paper. We first assume that the mass distribution is spherically symmetric. We also assume that the enclosed mass within the radius R is written by

$$M_R = m_1 + m_2 R^{1.25}. \quad (1)$$

where m_1 corresponds to the galactic center black hole, and the second term corresponds to the observed mass density distribution $\rho \propto R^{-1.75}$ (and the surface density mass distribution $\sigma(r) \propto r^{-0.75}$). In what follows, we will use cylindrical coordinates, r , ϕ , and z , where the z axis is taken along the line of sight to the galactic center (see figure 9). In this coordinate system, r is called the projected distance from the galactic center. The observed quantity, the average of v_z^2 between projected distances r_n and r_{n+1} , can be expressed using the Boltzmann one-particle distribution function, $f(r, \phi, z, v_r, v_\phi, v_z)$, as

$$\begin{aligned} & \left[\sum_{i}^{r_n < r_i < r_{n+1}} (v_{z,i})^2 \right] / N_n \\ & \simeq \int_{r_n}^{r_{n+1}} \int [(v_z)^2 f] dz r d\phi dv_r dv_z dv_\phi dr / \left[\int_{r_n}^{r_{n+1}} \int f dz r d\phi dv_r dv_z dv_\phi dr \right] \end{aligned} \quad (2)$$

where N_n is the number of the observed stars between r_n and r_{n+1} , and the subscript i indicates the i -th star in the sample. All the quantities on the right side of the equation are regarded as continuous functions of the coordinates, r , ϕ , z , v_r , v_z , and v_ϕ . A partial integration with respect to z in the numerator gives

$$\int_{r_n}^{r_{n+1}} \int [z(v_z)^2 f]_{z=-\infty}^{z=+\infty} r d\phi dv_r dv_z dv_\phi dr - \int_{r_n}^{r_{n+1}} \int [z v_z (v_z \partial f / \partial z)] dz r d\phi dv_r dv_z dv_\phi dr. \quad (3)$$

Here the first term vanishes because the function f tends to zero rapidly as z goes to infinity. Using the collisionless steady-state Boltzmann equation, the second integral can be related to the term $z v_z (F_z \partial f / \partial v_z)$. Details are given in the Appendix. Here the z component of the gravitational force F_z is given as $F_z = -GM_R z / R^3$, where G is the gravitational constant and $R = (z^2 + r^2)^{0.5}$. By integrating this equation over the line of sight and all the other coordinates with a density distribution

$$\rho(R) = \rho_0 R^{-1.75}, \quad (4)$$

and assuming a symmetric velocity distribution, we obtain the equation to be solved:

$$m_1 A_n + m_2 B_n = C_n, \quad (5)$$

where

$$A_n = 1.0245 G (r_{n+1}^{1/4} - r_n^{1/4}) / (r_{n+1}^{5/4} - r_n^{5/4}), \quad (6)$$

and

$$B_n = 0.7556 G (r_{n+1}^{3/2} - r_n^{3/2}) / (r_{n+1}^{5/4} - r_n^{5/4}), \quad (7)$$

$$C_n = \left(\sum_{i}^{r_n < r_i < r_{n+1}} v_{z,i}^2 \right) / N_n. \quad (8)$$

The unknowns, m_1 and m_2 , are solved by least squares with the set of A_n , B_n , and C_n ($n = 1, 2, \dots, n_e$), where n_e is the number of divided regions in the cylinder.

We calculated A_n , B_n , and C_n ($n = 1$ to 10) and solved m_1 and m_2 by least squares. In the present line-of-sight velocity sample of 199 SiO maser stars within 30 pc from the galactic center. In order to obtain accurate masses very near the galactic center, we added 10 SiO objects within $2'$ of the galactic center, as found by Deguchi et al. (2002). Furthermore, we excluded 5 extremely high velocity objects with $|v_{\text{lsr}}| > 200 \text{ km s}^{-1}$ from the fit. We divided the cylinder into 10 regions, where each has about 20 data points except the innermost cylinder which contains 10 points. The value of m_1 is somewhat sensitive to the velocity dispersion of the innermost 10 objects. In the case with no rotational motion ($V_{\text{Rot}} = 0$), we obtain

$$M_R = (2.69[\pm 1.30] + 0.53[\pm 0.07](R/\text{pc})^{1.25}) \times 10^6 M_\odot. \quad (9)$$

We can also involve the average rotational motion. Details are given in Appendix. Here we assume that the rotational velocity slowly increases with radius as $\sim r^{0.125}$. The average rotation speed can be obtained from the observational quantities and we obtain the rotational speed at 30 pc as $V_0 = 86.2 \text{ km s}^{-1}$. The mass distribution involving the rotation becomes

$$M_R = (2.69[\pm 1.30] + 0.88[\pm 0.07](R/\text{pc})^{1.25}) \times 10^6 M_\odot. \quad (10)$$

The thin and thick solid curves in figure 6 show the mass distributions for the non-rotating and rotating cases, respectively. These masses are slightly less than the values obtained using the other methods mentioned. Because of the self-consistency of this method, which uses only the line-of-sight velocities and the projected radii, we believe that the masses obtained in this paper are more accurate than those found previously. Also the effects of the foreground and background of the galactic center along the line of sight are correctly taken into account.

3.5. High Velocity Stars

We can clearly see five distinct high velocity stars with $|V_{\text{lsr}}| > 200 \text{ km s}^{-1}$ in figure 5. As noted before, these sources are located only on the $l^* < 0$ side, which is somewhat difficult to explain. However, because of their small numbers, we can always argue that their presence is accidental.

To understand the high velocity objects in greater detail, we consider the energetics of stars in the galactic center. The energy of a particle moving in the *fixed* gravitational potential can be written as

$$E/m = (1/2)v^2 + U(R), \quad (11)$$

where m and $U(R)$ are the mass of the particle and the gravitational potential at the radius, R , from the galactic center, respectively. Here, for convenience, we replace the term, E/m , by $U(R_0)$, where R_0 is the outermost radius to which the star can reach *if the orbit is linear*. Because the projected quantities, v_z^2 and r , are always smaller than v^2 and R , respectively, we have the inequalities

$$R \geq r, \quad (12)$$

and

$$2G^{-1}R[U(R_0) - U(R)] = G^{-1}Rv^2 \geq G^{-1}rv_z^2, \quad (13)$$

where G is the gravitational constant. Here, the quantity, $G^{-1}rv_z^2$ is often called the projected mass ($\equiv q$; Bahcall & Tremaine 1981). From the mass distribution of the galactic center (equation 1), we can compute the gravitational potential as

$$U(R) = G(-m_1 R^{-1} + 4m_2 R^{0.25}) \quad (14)$$

Note that $U(R)$ is a monotonically increasing function of R .

Figure 7 is a plot of the mass distribution, M_R , and the quantity $2G^{-1}R[U(R_0) - U(R)]$,

as a function of the real distance, R , for various different R_0 (indicated as the value R_0). We also plotted the projected mass q against projected radius r for the SiO-detected objects in figure 7 using the same axes. Because of the inequalities (12) and (13), the position of a star, $(R, G^{-1}Rv^2)$, must fall to the upper right part of the point $(r, G^{-1}rv_z^2)$ in figure 7. More precisely, it will be above the line connecting the origin and the point $(r, G^{-1}rv_z^2)$ and at the right part of the line $R=r$. In another words, the observed location of the projected quantities, (r, q) , gives the lower bound of $(R, 2G^{-1}R[U(R_0) - U(R)])$, in this diagram.

Note that a particle in a pure circular orbit in an edge-on plane (as viewed from the sun) falls on the curve M_R only when it moves along the line of sight. In general, the orbit of a particle is not edge-on, and the velocity vector is not along the line of sight. Therefore, the projected mass of a particle falls on a much lower part of the M_R curve. In summary, the particles at the upper-right part of the diagram in figure 7 have higher energy in general. But note that the particles with high $U(R)$ also fall towards the lower part of the diagram due to a projection effect; at best when $v_z = v$, the point, $(R, G^{-1}Rv^2)$, moves on a straight line through the origin.

With the help of the projected mass–radius diagram of figure 7, we can make subsamples of the set and investigate the statistical properties of the high $U(R_0)$ subsample. Let us divide the sample by the $q = 2G^{-1}r[U(30\text{pc}) - U(r)]$ curve and call the upper subset ($q > 2G^{-1}r(U(30\text{pc}) - U(r))$) as a high q subset. Note that this subset consist of the objects distributed over all the projected distances, but weighted more to the largest values. We tried to find statistical differences in K -magnitude and period between the high and low q subsets. However, no strong effects were found. If the stellar system is in equipartition of energy (though this is somewhat absurd in a collisionless system), the light mass particles may have larger specific energy E/m . However, we do not find any period or K -magnitude segregation effect on energy. Both luminosity and period are roughly increasing functions of stellar mass. Therefore, our finding, i.e., that the statistical properties of the two sets are similar, indicates that there is no strong mass segregation effect. Of course, the low- q subset is not purely one whose members have low energies but, in fact, comprises a mixture of stars with low and high $U(R_0)$ because of the projection effect. Therefore, it is understandable that they do not exhibit any strong differences in K and period statistics.

We can also divide the high q set into two; $V_{\text{lsr}} > 0$ and $V_{\text{lsr}} < 0$. This is because the SiO maser sample may exhibit a streaming motion of stars along the Bulge bar. Izumiura et al. (1995) demonstrated that the Bulge objects in front of the galactic center tend to exhibit a negative radial velocity and the objects behind a positive velocity, due to the streaming motions of stars in the bar-like Bulge. The same tendency was also observed in the sample of SiO maser stars within 3 degrees of the galactic center (Deguchi et al. 2000). This front and back effect may produce a systematic difference in the K magnitudes of the stars (Deguchi et al. 2002); the frontward stars must be systematically brighter than the background ones due to distance

or absorption by circumnuclear dust. Because the high- q objects are considered to be located in general (but not strictly always) outside $R=30$ pc, circumnuclear absorption is thought to have a significant influence on the K magnitudes.

Figure 8 shows a plot of K magnitude against period for the LAVs. The filled and unfilled circles indicate the objects with positive and negative V_{lsr} both with $q > 2G^{-1}r[U(30\text{pc}) - U(r)]$. Apparently, figure 8 indicates that the positive- V_{lsr} objects are fainter at K than the negative ones. The average K magnitudes are 9.44 (± 1.21) and 8.96 (± 0.79) for the 25 positive- and 25 negative-velocity sets respectively. The t- and F-tests give a probability of 11 % for the average K magnitude difference and a probability of 4 % for the standard-deviation difference being produced by the same distribution function. In other words, with more than 89% probability, two sets are statistically different. Therefore, if this average-magnitude difference is interpreted as being produced due to absorption by circumnuclear dust, the negative-velocity stars are in front of the galactic center and the positive-velocity stars are behind it.

We can recognize in figure 8 a slight shift in distribution of the two sets with respect to period. However, neither the t- nor the F-test gives any probability higher than 78 % for an average-period difference or a standard-deviation difference between the two sets. Therefore, we regard the period distributions in the two sets as being the same.

The systematic tendency towards brighter K -magnitude in the negative-velocity subset appears more strongly in the smaller subsets. For the top five high-velocity stars with $|V_{\text{lsr}}| > 190$ km s $^{-1}$, we obtain $K_{\text{ave}}=9.25$ (± 0.71) and $K_{\text{ave}}=8.23$ (± 0.30) for two positive and three negative high-velocity LAV stars. For the top 23 high- q stars, we obtain $K_{\text{ave}}=9.63$ (± 0.99) and $K_{\text{ave}}=8.93$ (± 0.94) for 11 positive and 12 negative high-velocity stars. Here the numbers in parentheses are standard deviations. Though these results are not statistically significant because of small samples, we believe that the tendency appears more drastically in the extremely high-velocity stars.

The above finding, i.e., that the negative-velocity stars are located relatively in front of and the positive-velocity stars behind the galactic center, indicates that they share the same dynamical property as the stars in the Bulge (Deguchi et al. 2001).¹ However, this fact does not immediately suggest that all of the high-velocity stars belong to the Bulge population and that their real distances from the galactic center are much farther than the projected distance, say about 30 pc. The average difference of 0.4 mag corresponds to a distance difference of about 1.5 kpc, if the magnitude difference is produced purely by distance effects. On the other hand, the distance difference is computed to be about 120 pc, when the extinction model of $A(K) \sim 3$ kpc $^{-1}$ is applied near the galactic center.

¹ It suggests that orbital motions of these stars are close to those of the x_1 orbit family in a bar potential (Binney & Merrifield 1998). Because the x_2 orbits are less elongated and have smaller orbital velocities than the x_1 orbits, the present high-velocity star subsample does not seem to show properties of the x_2 orbit family.

Though interstellar extinction by dust grains must have a strong influence on the K -magnitudes obtained, it is hard to quantify it because the dust distribution is irregular on scales of 1–5′ towards the galactic center. Because the present high- q objects are not concentrated in a particular region in the $24' \times 24'$ area, it is unthinkable that the above noted difference in the K -magnitudes is created only by the irregular distribution of the dust toward the galactic center.

The other notable point on the extremely high velocity stars is the lopsidedness of their distribution; all of the six extremely high-velocity stars with $|V_{\text{lsr}}| > 190 \text{ km s}^{-1}$ appear in the $l^* < 0$ side of the sky plane in the present sample. If we assume that an object should appear equally in both half-planes, the probability for all six to lie on one side of the plane is $1/32 \sim 3\%$. Of course, we can always argue that it is due to statistical fluctuations. In fact, we find an OH high-velocity source, OH 0.335–0.180 with $V_{\text{lsr}} = -355.1 \text{ km s}^{-1}$, on the $l^* > 0$ side of the plane in Sjouwerman et al. (1998), outside the present survey area.

The distribution of the circumnuclear molecular ring (Wright et al. 2001) is very asymmetric about Sgr A*, and the MSX 21 μm map in the same region shows heavy concentrations of bright objects on the $l^* > 0$ side (Price et al. 2001). Considering the dynamical (rotation) time scale of about 2 My, and the lifetime of molecular clouds of about 1–10 My, the lopsidedness of the interstellar matter can be regarded as a relatively short-lived phenomenon. The ages of AGB stars are between 30 My (about $9 M_{\odot}$) and 2 Gy (about $2 M_{\odot}$) (Vassiliadis, Wood 1993; Mouhcine, Lançon 2002). Therefore, such a lopsided distribution of the high velocity stars (if it is not a statistical fluctuation) may be more or less a reflection of an asymmetry of the gravitational potential. Kim et al. (2003) made a numerical simulation of the dynamical friction of stars in the central cluster within 30 pc and found that massive stars in a cluster can sink to the center within a relatively short time. By a counter-reaction, low-mass stars can be ejected from the cluster and can be observable as high-velocity stars. Though it is related to the disruption of young stellar clusters, the possible lopsided distribution of aged AGB high-velocity stars might be explained by a chance encounter of these AGB stars with such young clusters. However, we have not yet been able to reach a unified view of the high-velocity star phenomenon in the galactic center from the present data.

4. Conclusion

We have surveyed ~ 400 large-amplitude variables within a $24' \times 24'$ square about the galactic center, and obtained 180 detections (with additional 16 detections other than LAVs) in the SiO maser lines. The SiO detection rate of $\sim 48\%$ is comparable to that in previous SiO surveys of color-selected Bulge IRAS sources. The SiO detection rate increases with the period of light variation, and is well correlated with the OH detection rate. The longitude-velocity diagram of the SiO sources has been revealed to be quite similar to the OH l - v diagram. These facts suggest that the large-amplitude variables in the galactic nuclear disk are mass-losing

stars in the AGB phase, quite similar to the IRAS sources in the inner Galactic bulge.

We also analyzed the SiO radial velocity data and obtained the mass distribution of the galactic center area. The mass of the central black hole that we have deduced, $2.7(\pm 1.3) \times 10^6 M_\odot$, and the mass within 30 pc, $6.5(\pm 0.7) \times 10^7 M_\odot$, are more accurate than the previous estimates for these quantities. From analysis of the projected mass vs radius diagram, we found a tendency among the high-velocity sources that the subset with negative line-of-sight velocity is systematically brighter than the subset with positive line-of-sight velocity. This results from the fact that the the subsample with negative line-of-sight velocity is in front of the galactic center and the subsample with positive velocity is behind it. This tendency, which also applies to the Bulge SiO maser sources, strongly suggest the presence of streaming motion in the present nuclear-disk LAV sample.

The authors thank Dr. A. Winnberg for the useful comments. One of authors (I.S.G.) thanks the National Astronomical Observatory for providing him with a visiting fellowship for this work. This research was made use of the SIMBAD database operated at CDS, Strasbourg, France. It was partly supported by Scientific Research Grant (C2) 12640243 of the Japan Society for Promotion of Sciences.

Appendix. Theory for Computing the Enclosed Mass

We assume that the mass distribution is spherically symmetric. We also assume that the enclosed mass within the radius R is given by

$$M_R = m_1 + m_2 R^{1.25}, \quad (15)$$

where the first term corresponds to the mass of the central black hole, and the second term corresponds to the general mass density distribution (including dark matter) $\rho_R \sim R^{-1.75}$ (and the surface density mass distribution $\sigma(r) \sim r^{-0.75}$). Here, we adopt cylindrical coordinates, r , ϕ , and z , where the z axis is taken along the line of sight to the galactic center, r is the projected distance from the galactic center, and the direction of $\phi = 0$ to the galactic plane (see figure 9). The collisionless Boltzmann equation in a steady state can be written in cylindrical coordinates [for example, Binney & Tremaine (1987)]

$$v_r \partial f / \partial r + (v_\phi / r) \partial f / \partial \phi + v_z \partial f / \partial z + (v_\phi^2 / r + F_r) \partial f / \partial v_r - r^{-1} v_r v_\phi \partial f / \partial v_\phi + F_z \partial f / \partial v_z = 0, \quad (16)$$

where the ϕ component of the gravitational force F_ϕ vanishes because of the spherical symmetry. The average of v_z^2 in the area between r_n and r_{n+1} can be expressed using the Boltzmann one-particle distribution function, f , as

$$\begin{aligned} & \left[\sum_i^{r_n < r_i < r_{n+1}} (v_{zi})^2 \right] / N_n \\ & \simeq \int_{r_n}^{r_{n+1}} \int [(v_z)^2 f] dz r d\phi dv_r dv_z dv_\phi dr / \left[\int_{r_n}^{r_{n+1}} \int f dz r d\phi dv_r dv_z dv_\phi dr \right], \end{aligned} \quad (17)$$

where N_n is the number of stars observed between r_n and r_{n+1} , and the denominator is for

normalization. All the quantities on the right side of the equation are regarded as continuous functions of the coordinates, r , ϕ , z , v_r , v_ϕ , and v_z . The partial integral with respect to z can convert the numerator to

$$\int_{r_n}^{r_{n+1}} \int [z(v_z)^2 f]_{z=-\infty}^{z=+\infty} r d\phi dv_r dv_z dv_\phi dr - \int_{r_n}^{r_{n+1}} \int [z v_z (v_z \partial f / \partial z)] dz r d\phi dv_r dv_z dv_\phi dr, \quad (18)$$

Here the first integral vanishes because the distribution function f tends rapidly to zero at infinity. Using the collisionless steady-state Boltzmann equation (16), the second integral can be related to the term $z v_z (F_z \partial f / \partial v_z)$. Here the z component of the gravitational force F_z is given as $F_z = -GM_R z / R^3$ where $R = (z^2 + r^2)^{0.5}$. We perform the integral (18) over all the coordinates with a density distribution

$$\rho_R = \rho_0 R^{-1.75}. \quad (19)$$

Note that

$$\int_{-\infty}^{+\infty} f dv_r dv_z dv_\phi = \rho_R. \quad (20)$$

When the system is not rotating, further partial integral in expression (18) after the above noted replacement easily results in equation (5).

We have to involve the average rotational motion by the replacing

$$v_r = v_{0,r} + V_{\text{rot},r} \quad (21)$$

$$v_\phi = v_{0,\phi} + V_{\text{rot},\phi} \quad (22)$$

and

$$v_z = v_{0,z} + V_{\text{rot},z} \quad (23)$$

where $V_{\text{rot},r}$, $V_{\text{rot},\phi}$, and $V_{\text{rot},z}$ are the r , ϕ , and z , components of the rotational velocity. Here we assume the rotational axis is perpendicular to the galactic plane (i.e., perpendicular to z axis). We assume the rotational motion is fastest at equator, and gets slower according to a cosine law when approaching the pole (see figure 9). In such a case, the rotational velocity components can be written using the rotational velocity at the equator, V_{Rot} , as

$$V_{\text{rot},r} = -V_{\text{Rot}} z \cos(\phi) / R, \quad (24)$$

$$V_{\text{rot},\phi} = V_{\text{Rot}} z \sin(\phi) / R, \quad (25)$$

and

$$V_{\text{rot},z} = V_{\text{Rot}} r \cos(\phi) / R \quad (26)$$

(see figure 9). Here we assume that the rotational velocity V_{Rot} at the equator is given by the law corresponding to $\rho \sim R^{-1.75}$,

$$V_{\text{Rot}} = V_0 (R/r_0)^{0.125}, \quad (27)$$

where V_0 is the rotational velocity at the equator at $r_0 = 30$ pc. A more realistic case of V_{Rot} as a function of radius can also be calculated if the integral converges, but we do not pursue such a complex case here.

We perform integral (18) with respect to z , r , ϕ , $v_{0,z}$, $v_{0,r}$, and $v_{0,\phi}$, assuming that the distribution function is symmetric in z , $v_{0,z}$, $v_{0,r}$, and $v_{0,\phi}$ [for example, $f(r, \phi, z, v_{0,z}, v_{0,r}, v_{0,\phi}) = f(r, \phi, z, -v_{0,z}, v_{0,r}, v_{0,\phi})$]. In the partial integral, which must be made to convert the derivatives $\partial f/\partial r$, etc., to f , the odd terms of these variables vanish due to the symmetry. The only remaining terms come from the part, $z v_z F_z \partial f/\partial v_z$ (leading the term $m_1 A_n + m_2 B_n$), and the part (only in the rotational case), $z v_z v_r \partial f/\partial r$ (leading the term $V_0^2 D_n$). We obtain the equation to be solved:

$$m_1 A_n + m_2 B_n = C_n + V_0^2 D_n, \quad (28)$$

where where

$$A_n = 1.0245G (r_{n+1}^{1/4} - r_n^{1/4})/(r_{n+1}^{5/4} - r_n^{5/4}), \quad (29)$$

$$B_n = 0.7556G (r_{n+1}^{3/2} - r_n^{3/2})/(r_{n+1}^{5/4} - r_n^{5/4}), \quad (30)$$

$$C_n = \left(\sum_{i}^{r_n < r_i < r_{n+1}} v_{z,i}^2 \right) / N_n. \quad (31)$$

and

$$D_n = 0.5667G r_0^{-1/4} (r_{n+1}^{3/2} - r_n^{3/2})/(r_{n+1}^{5/4} - r_n^{5/4}), \quad (32)$$

The unknowns, m_1 and m_2 , are solved by least squares with the set of A_n , B_n , and C_n ($n = 1, 2, \dots, n_e$), where n_e is the total number of divided regions in the cylinder. The rotational term D_n appears due to the centrifugal force.

The average rotational velocity, V_0 , can be computed from the following equation;

$$\sum_i^{all} v_{zi} \cos(\phi_i) / N \simeq \int v_z \cos(\phi) f dr dz r d\phi dv_r dv_z dv_\phi / \left(\int f dr dz r d\phi dv_r dv_z dv_\phi \right), \quad (33)$$

where N is the total number of the observed particles and the integration must be made over all the coordinates. By integrating the right hand side after replacing v_z by equations (24) – (27), we get

$$V_0 = 3.726 \left[\sum_i^{all} v_{zi} \cos(\phi_i) \right] / N. \quad (34)$$

All the computations described above were made with help of computer-algebra software. A key aspect of the present analysis is that the functional form of the density distribution is given so that we can integrate the distribution function. The present analysis does not assume any special velocity distribution function except symmetry with respect to the velocities, $v_{0,z}$, $v_{0,r}$, and $v_{0,\phi}$. This is considered to be the same as an isotropic velocity distribution, though it is somewhat obscured because of the cylindrical coordinates.

In this method, the effect of the objects to the front and rear along the line of sight is correctly taken into account. Because of the self consistency, i.e., using only the line-of-sight velocities and projected radius, we believe that the mass distributions we have obtained are more accurate than those obtained with the projected-mass or pressure-balance methods [for the reference, see Bahcall & Tremaine (1981)].

References

- Bahcall, J. N., & Tremaine, S. 1981, *ApJ*, 244, 805
- Benson, P. J., & Little-Marenin, I. R. 1996, *ApJS*, 106, 579
- Benson, P. J.; Little-Marenin, I. R., Woods, T. C., Attridge, J. M., Blais, K. A., Rudolph, D. B., Rubiera, M. E., & Keefe, H. L. 1990, *ApJS*, 74, 911
- Binney, J., Gerhard, O. E., Stark, A. A., Bally, J., & Uchida, K. I. 1991, *MNRAS*, 252, 210
- Binney, J., & Merrifield, M. 1998, *Galactic Astronomy* (Princeton Univ. Press, Princeton), p588
- Binney, J., & Tremaine, S. 1987, *Galactic Dynamics* (Princeton Univ. Press, Princeton), p194
- Blitz, L., & Spergel, D. N. 1991, *ApJ*, 379, 631
- Deguchi, S., Fujii, T., Izumiura, H., Kameya, O., Nakada, Y., Nakashima, J., Otsubo, T., & Ukita, N. 2000, *ApJS*, 128, 571
- Deguchi, S., Fujii, T., Matsumoto, S. Nakashima, J., & Wood, P. 2001, *PASJ*, 53, 293
- Deguchi, S., Fujii, T., Miyoshi, M., & Nakashima, J. 2002, *PASJ*, 54, 61
- Dwek, E., Arendt, R. G., Hauser, M. G., Kelsall, T., Lisse, C. M., Moseley, S. H., Silverberg, R. F., Sodroski, T. J., & Weiland, J. L. 1995, *ApJ*, 445, 716
- Genzel, R., Pichon, C., Eckart, A., Gerhard, O. E., & Ott, T. 2000, *MNRAS*, 317, 348
- Ghez, A. M., Morris, M., Becklin, E. E., Tanner, A., & Kremenek, T. 2000, *Nature*, 407, 349
- Glass, I. S., Matsumoto, S., Carter, B. S., & Sekiguchi, K. 2001, *MNRAS* 321, 77 (Erratum: *MNRAS* 336, 1390)
- Hozumi, S. Burkert, A. Fujiwara, T. 2000, *MN*, 311, 377
- Imai, H., Deguchi, S., Fujii, T., Glass, I. S., Ita, Y., Izumiura, H., Kameya, O., Miyazaki, A., Nakada, Y., & Nakashima, J., 2002, *PASJ*, 54, L19
- Izumiura, H., Deguchi, S., Hashimoto, O., Nakada, Y., Onaka, T., Ono, T., Ukita, N., & Yamamura, I. 1995, *ApJ*, 453, 837
- Kim, S.S., Figer, D.F. & Morris, M. 2003, *Astron. Nachr.* 324 (in press) : paper presented in the Galactic Center Workshop GC2002
- Lindqvist, M., Habing, H. J., & Winnberg, A. 1992, *A&A*, 259, 118
- Levine, D., Figer, D. F., Morris, M., & McLean, I. S., 1995, *ApJ*, 447, L101
- Menten, K. M., Reid, M. J., Eckart, A., & Genzel, R. 1997, *ApJ*, 475, L111
- Messineo, M., Habing, H. J., Sjouwerman, L. O., Omont, A., & Menten, K. M. 2002, *A&A*, 393, 115
- Miyazaki, A., Deguchi, S., Tsuboi, M., Kasuga, T., & Takano, S., 2001, *PASJ*, 53, 501
- Mouhcine, M., & Lançon, A. 2002, *A&A*, 393, 149
- Morris, M., & Serabyn, E. 1996, *ARA&A*, 34, 645

Nakada, Y., Deguchi, S., Hashimoto, O., Izumiura, H., Onaka, T., Sekiguchi, K., & Yamamura, I. 1991, *Nature*, 353, 140

Oka, T., Hasegawa, T., Sato, F., Tsuboi, M., & Miyazaki, A. 1998, *ApJS*, 118, 445

Omont, A., Gilmore, G. F., Alard, C., Aracil, B., August, T., et al. 2003 *A&A*, 403, 975

Price, S. D., Egan, M. P., Carey, S. J., Mizuno, D. R., & Kuchar, T. A. 2001, *AJ*, 121, 2819

Philipp, S., Zylka, R., Mezger, P. G., Duschl, W. J., Herbst, T., & Tuffs, R. J. 1999, *A&A*, 348, 768

Reid, M. J., Menten, K. M., Genzel, R., Ott, T., Schöel, R., Eckart, A. 2003, *ApJ*, 587, 208

Rogers, A. E. E., Doeleman, S., Wright, M. C. H., Bower, G. C., Backer, D. C., Padin, S., Philips, J. A., Emerson, D. T., et al. 1994, *ApJ*, 434, L59

Saha, P., Bicknell, G. V., & McGregor, P. J. 1996, *ApJ*, 467, 636

Sellgren, K., Hall, D. N. B., Kleinmann, S. G., & Scoville, N. Z., 1987, *ApJ*, 317, 881

Shlosman, I. Frank, J. & Begelman, M. C. 1989, *Nature*, 338, 45

Sjouwerman, L. O., van Langevelde, H. J., Winnberg, A., & Habing, H. J. 1998, *A&AS*, 128, 35

Sjouwerman, L. O., Lindqvist, M., van Langevelde, H. J., & Diamond, P. J. 2002, *A&A*, 391, 967

Taylor, G. B., Morris, M., Schulman, E. 1993, *AJ*, 106, 1978

Tsuboi, M., Handa, T., & Ukita, N. 1999, *ApJS*, 120, 1

van Langevelde, H. J., Brown, A. G. A., Lindqvist, M., Habing, H. J., & de Zeeuw, P. T. 1992, *A&A*, 261, L17

Vassiliadis, E., & Wood, P. R. 1993, *ApJ*, 413, 641

Weiner, B. J., Sellwood, J. A. 1999, *ApJ*, 524, 112

Wood, P. R., Habing, H. J., & McGregor, P. J. 1998, *A&A*, 336, 925

Wright, M. C. H., Coil, A. L., McGary, R. S., Ho, P. T. P., & Harris, A. I. 2001, *ApJ*, 551, 254

Table 1. additional stars observed

Name	R. A. (J2000) Dec.						P (d)	K_{av} (mag)	A (mag)	comment
	h	m	s	°	'	"				
6-154	17	45	48.6	-29	09	55.8	—	—	—	erratic possibly double
7-389	17	45	59.7	-29	02	43.4	362	10.5	1.5	
23-255	17	45	00.6	-28	59	54.7	426	10.4	1.3	

Table 2. SiO detections

name	SiO $J = 1-0$ $v = 1$						SiO $J = 1-0$ $v = 2$				Obs. Date (yymmdd.d)
	l ($^{\circ}$)	b ($^{\circ}$)	V_{peak} (km s^{-1})	T_{peak} (K)	Flux (K km s^{-1})	RMS (K)	V_{peak} (km s^{-1})	T_{peak} (K)	Flux (K km s^{-1})	RMS (K)	
1-2	0.089	0.007	-32.3	0.093	0.074	0.034	-30.5	0.185	0.087	0.035	020309.2
1-8	0.095	-0.007	79.1	0.417	1.342	0.049	79.0	0.335	0.707	0.050	010220.3
1-31	0.113	0.063	-39.2	0.183	0.726	0.038	-38.0	0.146	0.561	0.043	010311.2
1-42.1	0.074	0.023	43.5	0.133	0.346	0.041	44.0	0.132	0.175	0.043	020525.1
1-42.2	0.074	0.023	57.3	0.109	0.027	0.041	57.3	0.114	0.294	0.043	020525.1
1-72	0.064	-0.006	21.0	0.374	1.310	0.040	21.2	0.232	0.967	0.042	010311.2
1-391	0.072	-0.011	94.1	0.321	0.566	0.053	94.3	0.335	0.529	0.058	020224.2
1-1890	0.083	0.063	23.3	0.235	0.423	0.036	23.9	0.275	1.065	0.038	010308.2
2-1	359.999	-0.004	-6.1	0.501	1.804	0.050	-5.7	0.420	1.742	0.045	010309.2
2-3	359.964	0.007	-7.6	0.343	0.839	0.041	-7.5	0.360	0.837	0.041	010223.2
2-9	0.004	-0.014	86.0	0.149	0.385	0.044	91.3	0.153	0.683	0.048	020314.3
2-10 †	0.003	-0.004	-6.7	0.193	0.377	0.040	-7.1	0.188	0.568	0.044	020423.2
2-11.1	359.997	-0.009	-23.0	0.271	0.500	0.047	-23.0	0.266	0.184	0.052	020527.0
2-11.2 †	359.997	-0.009	-7.1	0.144	0.524	0.047	-6.2	0.187	0.440	0.052	020527.0
2-18	359.967	0.002	-7.0	0.512	1.953	0.056	-9.7	0.453	2.218	0.059	020308.2
2-26.1	359.990	-0.011	-66.5	0.117	0.498	0.036	-61.3	0.160	0.359	0.038	020314.2
2-26.2	359.990	-0.011	151.5	0.176	0.457	0.037	151.6	0.186	0.421	0.047	020314.2
2-28	0.037	-0.003	35.1	0.206	0.598	0.054	36.9	0.218	0.354	0.049	010520.0
2-43	0.007	-0.038	110.9	0.705	1.099	0.051	111.0	0.531	0.845	0.052	020521.0
2-49	0.049	-0.005	63.6	0.174	0.264	0.042	64.0	0.177	0.184	0.043	020522.1
2-52	359.996	0.015	113.7	0.131	0.392	0.036	112.5	0.098	0.259	0.036	010309.3
2-320	0.060	-0.018	-4.7	0.274	0.766	0.041	-4.6	0.230	0.815	0.039	020309.2
2-697	0.025	0.027	-53.2	0.286	0.727	0.071	-51.7	0.246	0.373	0.071	010522.0
2-6329	0.015	-0.046	114.7	0.196	1.225	0.039	118.8	0.142	0.980	0.040	010222.3
3-5.1 †	359.957	-0.050	36.5	0.120	0.340	0.037	35.2	0.192	0.463	0.037	010218.3
3-5.2	359.957	-0.050	51.5	0.146	0.770	0.035	54.2	0.166	0.474	0.037	010218.3
3-6	359.970	-0.043	22.4	0.213	0.575	0.041	23.5	0.323	1.129	0.041	010308.2
3-16	359.954	-0.054	32.0	0.184	0.147	0.047	33.7	0.235	0.630	0.052	030522.0
3-49.1 †	359.905	-0.036	-140.9	0.231	0.556	0.047	-140.8	0.247	0.787	0.051	020424.1
3-49.2	359.905	-0.036	-98.7	0.178	0.225	0.047	—	—	—	0.045	020424.1
3-49.3 †	359.905	-0.036	-46.9	0.192	0.677	0.044	-50.6	0.174	1.072	0.045	020424.1
3-57	359.914	-0.042	-21.6	0.218	0.236	0.053	-23.6	0.280	0.667	0.058	030514.1
3-72 †	359.944	-0.049	-27.6	0.313	0.893	0.047	-27.9	0.258	0.745	0.047	020424.1

Table 2. (Continued)

3-88.1	359.932	-0.045	-115.5	0.149	0.507	0.046	-114.2	0.154	0.418	0.044	030510.0
3-88.2	359.932	-0.045	8.2	0.242	0.439	0.046	8.5	0.188	0.583	0.044	030510.0
3-101 †	359.965	-0.043	24.2	0.343	1.055	0.061	23.7	0.362	1.147	0.059	020524.1
3-108	359.902	-0.045	-141.3	0.160	0.327	0.061	-141.3	0.324	0.561	0.069	030514.1
3-205 †	359.933	-0.059	-93.6	0.214	0.300	0.071	-93.7	0.256	0.040	0.076	020519.0
3-220	359.910	-0.043	—	—	—	0.075	-142.1	0.282	0.325	0.094	020520.1
3-226	359.946	-0.092	134.2	0.247	0.331	0.058	134.2	0.204	0.016	0.069	010519.1
3-247	359.910	-0.028	-45.2	0.387	1.330	0.067	-44.7	0.347	0.843	0.064	020520.1
3-266	359.938	-0.009	-73.7	0.424	1.274	0.064	-72.3	0.259	0.557	0.055	010522.1
3-358	359.986	-0.061	13.3	0.264	0.923	0.044	12.4	0.264	0.818	0.045	010223.3
3-779.1	359.906	-0.041	-141.6	0.117	0.252	0.030	-141.8	0.135	0.382	0.037	010309.2
3-779.2 †	359.906	-0.041	-46.9	0.190	0.986	0.037	-48.2	0.149	0.538	0.037	010309.2
3-885	359.955	-0.030	66.3	0.101	0.181	0.034	65.5	0.141	0.345	0.036	020305.2
3-2389	359.939	-0.052	53.8	0.161	0.361	0.045	54.2	0.315	0.611	0.052	020221.4
3-2752	359.985	-0.042	5.8	0.142	0.468	0.041	5.5	0.183	0.277	0.039	010520.0
3-2855	359.918	-0.055	-308.0	0.227	0.558	0.060	-308.2	0.250	0.351	0.068	010519.1
3-4969	359.999	-0.061	107.7	0.184	0.641	0.049	109.5	0.199	0.825	0.056	020423.1
3-7655	359.967	0.002	-7.6	0.447	1.210	0.044	-7.5	0.359	1.416	0.042	010519.0
4-6.1	359.858	-0.056	-20.1	0.120	0.234	0.030	—	—	—	0.033	020312.2
4-6.2 †	359.858	-0.056	8.8	0.093	0.514	0.030	6.2	0.114	0.377	0.033	020312.2
4-23	359.857	-0.060	3.4	0.184	0.215	0.038	3.4	0.176	0.652	0.038	010223.3
4-28	359.860	-0.067	5.4	0.172	0.216	0.044	—	—	—	0.048	030525.1
4-33	359.899	-0.068	-34.1	0.124	0.641	0.041	-35.1	0.225	0.902	0.056	040225.2
4-113 †	359.855	-0.078	—	—	—	0.042	-289.4	0.164	0.710	0.051	010219.3
4-253	359.909	-0.113	-46.7	0.225	0.586	0.055	-45.4	0.171	0.235	0.046	010521.0
4-340	359.888	-0.051	-55.6	0.225	1.048	0.044	-55.1	0.228	1.072	0.049	020224.3
4-557	359.902	-0.103	-85.2	0.252	0.838	0.034	-85.0	0.287	0.955	0.036	010219.3
5-10	359.814	-0.162	-31.8	0.259	0.749	0.049	-30.3	0.187	0.832	0.047	020220.2
5-27 ‡	359.819	-0.116	-101.7	0.208	0.490	0.054	-100.0	0.249	0.728	0.053	020220.4
5-91	359.837	-0.156	91.1	0.238	0.860	0.038	91.0	0.155	0.475	0.036	020309.2
5-157.1	359.820	-0.101	-2.3	0.156	0.434	0.031	—	—	—	0.029	020310.2
5-157.2	359.820	-0.101	6.9	0.109	0.298	0.031	6.6	0.097	0.277	0.029	020310.2
5-2856	359.777	-0.119	71.0	0.134	0.078	0.036	—	—	—	0.035	010404.2
6-20	359.970	-0.111	-7.5	0.314	1.058	0.065	-8.8	0.369	1.032	0.067	020519.1
6-22	0.001	-0.124	6.6	0.153	0.355	0.043	5.2	0.139	0.193	0.043	020424.1
6-25	0.013	-0.117	-1.6	0.143	0.318	0.042	-0.1	0.181	0.329	0.042	010223.2
6-36	359.998	-0.117	75.9	0.100	0.252	0.032	77.7	0.112	0.322	0.034	020221.3

Table 2. (Continued)

6-44	359.983	-0.158	12.0	0.113	0.187	0.046	14.1	0.193	0.395	0.049	030525.0
6-85	0.002	-0.068	88.0	0.166	0.549	0.052	88.1	0.199	0.217	0.053	010522.1
6-112	359.969	-0.124	—	—	—	0.053	-8.7	0.179	1.000	0.056	030514.1
6-135	0.007	-0.089	5.9	0.174	0.613	0.042	5.7	0.193	0.526	0.040	010308.2
6-151 ‡	0.027	-0.128	-17.6	0.102	0.158	0.030	-23.7	0.075	0.027	0.032	030517.1
6-247	359.946	-0.098	134.1	0.208	0.366	0.037	134.3	0.158	0.354	0.041	020310.2
7-9	359.943	-0.154	-25.6	0.147	0.278	0.035	-26.4	0.215	0.447	0.041	020308.2
7-13	359.890	-0.151	5.7	0.186	0.464	0.038	4.8	0.235	1.145	0.037	010223.3
7-20	359.905	-0.159	-55.8	0.522	4.290	0.044	-55.5	0.539	5.543	0.039	010219.2
7-52	359.940	-0.194	-27.0	0.182	0.503	0.213	-32.2	0.130	0.366	0.049	030525.1
8-2 ‡	359.893	-0.216	-18.0	0.143	0.515	0.039	-19.4	0.169	0.652	0.039	020525.0
8-8	359.868	-0.232	30.2	0.168	0.353	0.049	31.1	0.198	0.510	0.050	020425.1
8-23	359.836	-0.177	-84.6	0.099	0.296	0.029	-82.3	0.082	0.241	0.028	020310.2
8-31	359.817	-0.206	109.6	0.115	0.149	0.033	107.3	0.113	0.163	0.047	010404.2
8-53	359.851	-0.221	-27.6	0.161	0.210	0.049	-26.7	0.126	0.054	0.047	010527.1
9-8.1	0.041	-0.060	-4.4	0.283	1.168	0.038	-4.4	0.228	0.965	0.041	010223.4
9-8.2 †	0.041	-0.060	72.5	0.184	0.350	0.038	72.7	0.273	0.368	0.041	010223.4
9-9	0.071	-0.053	21.2	0.149	0.410	0.038	25.0	0.137	0.753	0.037	010309.3
9-49	0.053	-0.063	-14.0	0.157	0.543	0.037	-14.0	0.108	0.548	0.041	020223.3
9-54	0.063	-0.057	26.0	0.264	0.538	0.072	24.6	0.254	0.470	0.075	020519.0
9-67	0.079	-0.103	-28.3	0.174	0.390	0.040	-28.3	0.121	0.450	0.044	020423.2
9-94	0.076	-0.108	55.2	0.088	0.447	0.034	57.7	0.123	0.346	0.033	020526.1
9-144	0.047	-0.116	59.3	0.217	0.281	0.044	60.1	0.198	0.124	0.047	020314.3
9-547.1 †	0.040	-0.056	-4.0	0.242	0.528	0.049	-3.8	0.296	0.804	0.052	020524.0
9-547.2	0.040	-0.056	73.0	0.212	0.332	0.049	72.0	0.231	0.390	0.052	020524.0
10-5	0.112	-0.080	69.7	0.178	0.432	0.050	70.3	0.162	0.167	0.050	010220.3
10-6	0.108	-0.016	39.5	0.517	2.081	0.052	39.6	0.361	1.445	0.050	010222.2
10-13	0.103	-0.052	55.3	0.173	0.268	0.055	54.2	0.231	0.964	0.057	020530.0
10-26	0.172	-0.046	-66.7	0.147	0.354	0.054	-65.0	0.210	0.351	0.052	020528.1
10-27	0.154	-0.051	-85.8	0.113	0.572	0.038	-86.3	0.107	0.428	0.039	020316.2
10-40	0.131	-0.059	-29.0	0.286	0.745	0.057	-29.9	0.279	0.550	0.055	020424.2
10-45	0.120	-0.005	106.3	0.222	0.582	0.040	105.4	0.180	0.560	0.041	020316.2
10-84	0.115	-0.043	-28.1	0.233	0.514	0.043	-27.6	0.345	0.587	0.045	010221.2
10-392	0.129	-0.020	93.8	0.185	0.512	0.039	94.8	0.167	0.246	0.039	010308.2
11-15	0.034	-0.146	98.4	0.185	0.472	0.044	99.4	0.170	0.387	0.046	020526.0
11-23	0.081	-0.187	1.1	0.181	0.425	0.041	2.2	0.147	0.459	0.045	020423.2
11-241	0.048	-0.159	55.9	0.155	0.514	0.047	54.6	0.154	0.135	0.047	020527.0

Table 2. (Continued)

11-4503	0.009	-0.174	8.0	0.113	0.117	0.040	7.8	0.203	0.293	0.041	010520.0
12-4	0.060	-0.132	-11.5	0.161	0.809	0.053	-16.4	0.128	0.437	0.056	020522.1
12-6 ‡	0.090	-0.174	6.1	0.100	0.280	0.036	4.0	0.156	0.556	0.041	030529.0‡
12-13	0.108	-0.097	-19.4	0.325	1.602	0.065	-19.7	0.345	1.506	0.071	010522.0
12-19	0.132	-0.137	41.8	0.307	0.759	0.075	41.7	0.284	0.389	0.073	020519.0
12-21.1	0.091	-0.123	32.5	0.102	0.269	0.040	33.9	0.116	0.209	0.040	010223.4
12-21.2 †	0.091	-0.123	70.2	0.147	0.503	0.040	72.7	0.161	0.036	0.040	010223.4
12-51	0.138	-0.137	44.5	0.333	0.976	0.046	44.2	0.545	1.610	0.048	010221.2
12-65	0.088	-0.119	74.5	0.167	0.434	0.039	—	—	—	0.043	020223.3
12-79	0.075	-0.123	—	—	—	0.404	35.9	0.167	0.359	0.062	020528.1
12-145	0.068	-0.123	33.3	0.231	1.122	0.049	35.7	0.230	0.588	0.047	020223.3
12-228	0.129	-0.145	-74.2	0.240	0.797	0.039	-74.3	0.191	0.355	0.041	010404.2
12-352	0.062	-0.136	-10.2	0.260	0.722	0.062	-16.0	0.176	0.493	0.057	020523.0
12-1236	0.121	-0.112	41.4	0.212	0.190	0.054	42.1	0.162	0.275	0.055	020530.1
13-16	0.179	-0.108	85.7	0.382	1.198	0.063	80.7	0.237	0.892	0.058	010526.0
13-18	0.158	-0.063	16.3	0.340	0.758	0.052	16.2	0.305	0.930	0.050	010526.0
13-55	0.167	-0.060	37.5	0.308	0.742	0.039	37.3	0.211	0.640	0.042	010311.2
13-200	0.178	-0.053	23.4	0.250	0.729	0.045	24.0	0.195	0.925	0.043	010521.0
14-2	359.944	-0.233	-58.7	0.344	1.258	0.065	-58.6	0.285	0.997	0.061	010520.1
14-6	359.972	-0.193	-34.4	0.181	0.837	0.036	-30.5	0.196	0.839	0.036	010219.3
14-11	359.949	-0.237	-59.0	0.245	0.601	0.059	-61.2	0.250	0.606	0.062	010526.1
14-38	359.947	-0.228	-57.7	0.216	0.760	0.054	-56.3	0.264	1.332	0.059	020528.0
16-1.1 †	359.867	0.027	-5.1	0.184	0.144	0.036	-5.3	0.196	0.426	0.035	010309.2
16-1.2	359.867	0.027	22.4	0.194	0.821	0.036	21.9	0.115	0.706	0.035	010309.2
16-5	359.904	-0.022	14.6	0.155	0.442	0.041	14.7	0.222	0.843	0.044	020525.0
16-8	359.953	0.011	-46.7	0.223	0.937	0.035	-47.5	0.186	0.969	0.037	010404.1
16-15	359.943	0.005	-57.6	0.219	0.230	0.044	-54.9	0.125	0.337	0.045	020526.0
16-25	359.929	0.037	-60.8	0.335	1.132	0.039	-61.5	0.175	0.857	0.036	010218.3
16-28	359.891	-0.026	-54.5	0.109	0.391	0.031	-54.4	0.150	0.357	0.033	020312.2
16-29	359.924	0.000	47.2	0.105	0.284	0.035	46.6	0.122	0.430	0.035	020311.2
16-36	359.925	0.015	51.2	0.258	1.105	0.044	49.3	0.238	0.937	0.043	010223.3
16-47	359.890	0.038	-12.6	0.177	0.480	0.044	-11.8	0.142	0.149	0.044	020221.4
16-49	359.938	-0.010	-72.0	0.173	0.660	0.037	-73.2	0.214	0.990	0.041	020308.2
16-77.1	359.924	-0.007	-28.2	0.137	0.350	0.035	—	—	—	0.036	020220.3
16-77.2	359.924	-0.007	246.8	0.126	0.501	0.040	241.6	0.195	0.877	0.045	020220.3
16-98	359.901	0.013	-26.4	0.181	0.595	0.046	-33.2	0.188	0.588	0.048	030522.0
16-286	359.885	0.016	-31.6	0.185	0.734	0.041	-31.6	0.169	0.241	0.040	020424.1

Table 2. (Continued)

17-1	359.963	0.007	-9.8	0.212	0.652	0.049	-6.8	0.247	1.088	0.051	020521.0
17-5	359.950	0.078	-48.2	0.101	0.264	0.034	—	—	—	0.037	020314.2
17-8	359.935	0.058	-36.6	0.188	0.281	0.044	-36.6	0.192	0.689	0.048	020314.3
17-9	359.977	0.031	-41.6	0.193	0.231	0.049	-42.4	0.181	0.400	0.048	020524.0
17-34	0.011	0.044	77.6	0.219	0.537	0.044	—	—	—	0.047	030523.1
17-95	0.006	0.042	0.6	0.117	0.147	0.041	-0.2	0.104	0.419	0.041	030522.0
17-118	0.007	0.046	77.9	0.235	0.338	0.071	77.8	0.225	0.889	0.072	020519.0
17-630	359.948	0.066	-9.5	0.412	1.217	0.038	-10.0	0.393	1.210	0.037	010222.3
17-3762	359.990	0.030	-49.2	0.322	0.857	0.036	-48.8	0.327	0.916	0.038	010221.3
18-14	0.020	0.106	-38.5	0.191	0.318	0.051	-39.6	0.155	0.136	0.050	010220.3
18-74	0.051	0.079	121.5	0.128	0.433	0.037	121.1	0.136	0.224	0.042	020305.3
18-173	0.042	0.082	72.6	0.136	0.243	0.056	73.5	0.275	0.710	0.056	020224.2
18-190.1	0.075	0.085	-48.8	0.169	0.479	0.053	-47.3	0.132	0.365	0.054	030510.1
18-190.2	0.075	0.085	100.9	0.370	1.059	0.053	102.3	0.364	1.162	0.054	030510.1
19-2	359.805	0.000	-18.2	0.200	0.899	0.041	-17.3	0.255	1.849	0.040	010219.2
19-7.1 †	359.848	-0.007	-107.5	0.106	0.294	0.035	-103.7	0.144	0.436	0.036	010219.3
19-7.2	359.848	-0.007	-34.2	0.191	0.729	0.035	-29.6	0.134	0.506	0.036	010219.3
19-9	359.845	-0.010	-33.4	0.284	0.977	0.080	-37.7	0.328	0.486	0.076	020529.0
19-48	359.849	0.009	-98.6	0.274	0.552	0.062	-98.3	0.237	0.659	0.063	020520.1
19-476	359.797	-0.026	-75.5	0.215	0.523	0.056	-74.4	0.209	0.160	0.052	010526.1
19-582	359.825	-0.024	-50.2	0.144	0.136	0.033	—	—	—	0.048	020310.3
19-685.1 †	359.869	-0.018	-52.8	0.350	1.308	0.074	-54.1	0.343	0.554	0.069	010522.0
19-685.2	359.869	-0.018	-44.0	0.330	0.896	0.074	-44.3	0.258	0.860	0.069	010522.0
19-780	359.810	-0.045	-43.3	0.174	0.600	0.039	-45.5	0.167	0.271	0.040	020309.3
20-11	359.730	-0.054	-31.4	0.189	0.507	0.052	-36.4	0.163	0.532	0.050	020522.0
20-26	359.810	-0.070	-37.7	0.130	0.688	0.033	-39.1	0.151	0.491	0.034	010220.2
20-74	359.772	-0.078	-76.4	0.348	1.084	0.061	-74.3	0.279	0.978	0.057	020522.0
20-116	359.751	-0.077	-21.4	0.223	0.925	0.058	-14.6	0.240	0.495	0.052	020528.0
20-136	359.791	-0.081	-96.2	0.384	1.541	0.050	-94.6	0.340	1.759	0.047	010309.3
20-2631 ‡	359.799	-0.090	-1.4	0.127	0.360	0.039	-6.5	0.164	0.578	0.040	020525.0
21-6	359.714	-0.014	91.1	0.288	0.394	0.054	90.9	0.234	0.572	0.055	020530.0
21-12	359.760	-0.000	-20.6	0.173	0.167	0.048	-18.8	0.193	0.471	0.044	010527.1
21-17	359.689	-0.004	317.2	0.196	0.440	0.057	317.8	0.292	0.221	0.064	020522.0
21-27	359.740	0.002	-68.3	0.089	0.437	0.030	-69.0	0.075	0.107	0.030	020310.2
21-39	359.742	0.006	-65.1	0.437	2.189	0.036	-65.2	0.272	1.528	0.032	010220.2
22-4	359.838	0.052	-68.7	0.349	0.603	0.040	-68.6	0.236	0.489	0.039	010218.2
22-7	359.790	0.034	-66.7	0.141	0.470	0.041	-69.3	0.209	0.586	0.038	010223.3

Table 2. (Continued)

22-9	359.823	0.056	84.2	0.126	0.432	0.035	86.0	0.175	0.586	0.036	020310.2
22-11	359.801	0.017	-195.8	0.275	0.820	0.057	-198.8	0.250	0.340	0.067	010522.0
22-21.1	359.830	0.047	12.0	0.166	0.244	0.031	12.1	0.098	0.342	0.032	020312.2
22-21.2	359.830	0.047	156.9	0.141	0.369	0.033	155.5	0.192	0.330	0.039	020312.2
22-21.3	359.830	0.047	165.1	0.124	0.352	0.033	166.0	0.180	0.354	0.039	020312.2
22-22	359.796	0.021	-12.0	0.177	0.273	0.049	-10.8	0.178	0.342	0.047	010521.0
22-27	359.773	0.017	43.1	0.339	0.931	0.058	43.1	0.233	0.374	0.060	030511.1
22-35	359.786	0.007	-78.2	0.167	0.459	0.044	-76.4	0.209	0.558	0.047	020312.3
22-76	359.837	0.030	-75.4	0.178	0.407	0.050	-79.2	0.113	0.095	0.042	010521.1
22-166	359.771	0.044	-139.0	0.183	0.315	0.038	-139.2	0.313	0.429	0.045	020309.3
22-274 †	359.778	0.010	-81.2	0.180	0.255	0.052	—	—	—	0.050	010309.3
23-5	359.865	0.126	-5.4	0.174	0.799	0.035	1.2	0.114	0.458	0.036	010218.3
23-7	359.862	0.052	-140.1	0.218	0.499	0.044	-142.7	0.151	0.328	0.051	030513.1
23-8	359.890	0.114	-109.3	0.125	0.183	0.034	-108.7	0.132	0.234	0.045	010404.1
23-10.1	359.864	0.055	-299.5	0.125	0.207	0.033	-299.3	0.163	0.350	0.039	020221.3
23-10.2 †	359.864	0.055	-141.1	0.112	0.215	0.033	-138.5	0.105	0.022	0.040	020221.3
23-22	359.869	0.099	-33.8	0.369	0.716	0.066	-33.4	0.336	0.908	0.081	020311.3
23-37	359.859	0.068	-130.2	0.160	0.222	0.032	-130.8	0.178	0.296	0.040	020311.2
23-101	359.902	0.061	-132.1	0.287	0.565	0.037	-131.9	0.283	0.644	0.044	020308.2
23-255	359.877	0.081	24.8	0.154	0.133	0.049	24.9	0.177	0.477	0.053	030528.0
23-1198	359.917	0.083	65.8	0.356	1.302	0.066	62.8	0.294	1.509	0.067	030525.0
24-108	359.925	0.124	-2.6	0.116	0.154	0.037	—	—	—	0.039	030522.0
25-9	0.024	0.143	-0.4	0.187	0.394	0.046	-0.9	0.157	0.426	0.050	030514.0
25-23	359.993	0.175	-2.9	0.178	0.432	0.043	-0.2	0.121	0.297	0.043	030510.1
25-234	0.018	0.156	105.3	0.244	0.821	0.080	104.5	0.337	0.806	0.065	030526.0

† a contamination from the other source; see the assignment in table 5.

‡ Off-position detection at the other velocity.

§ maybe multiple detections.

‡ reobserved on the day different from that shown in figure 2f.

Table 3. Negative results

GMCS Name	l	b	RMS($v = 1$)	RMS($v = 2$)	ObsDate1	ObsDate2
	($^{\circ}$)	($^{\circ}$)	(K)	(K)	(yymmdd.d)	(yymmdd.d)
1-19	0.122	0.049	0.041	0.040	020522.1	010525.1
1-26	0.095	0.075	0.066	0.062	020224.3	010526.0
1-37	0.074	0.015	0.047	0.047	020524.0	010522.0
1-41	0.086	0.056	0.048	0.051	010526.0	020520.0
1-46	0.060	0.017	0.046	0.046	010221.2	020424.2
1-175	0.066	0.007	0.056	0.054	010525.1	020521.1
1-182	0.072	0.019	0.051	0.047	030514.0	—
2-13	0.047	0.014	0.044	0.039	030519.1	—
2-27	0.003	-0.019	0.100	0.102	020219.3	—
2-30	359.993	-0.037	0.046	0.042	020526.0	—
2-46	359.986	-0.019	0.032	0.029	030517.1	—
2-58	359.976	-0.009	0.033	0.033	020526.1	—
2-79	0.016	-0.035	0.042	0.041	030510.1	—
2-145	359.978	0.015	0.053	0.052	030522.1	—
2-147	0.056	-0.024	0.040	0.037	030522.0	—
2-504	0.030	-0.026	0.069	0.065	020519.1	—
3-3‡	359.970	-0.049	0.040	0.035	010404.1	—
3-50	359.950	-0.015	0.058	0.058	020519.1	—
3-61	359.937	-0.025	0.049	0.048	020529.0	—
3-116	359.921	-0.030	0.061	0.119	030525.0	—
3-131	359.947	-0.015	0.053	0.049	030525.1	—
3-270	359.935	-0.040	0.060	0.116	030526.0	—
3-271	359.929	-0.014	0.032	0.032	020221.3	—
3-300	359.927	-0.018	0.047	0.041	030513.1	—
4-9	359.834	-0.091	0.047	0.044	020312.3	—
4-17	359.911	-0.103	0.056	0.050	030511.0	—
4-22	359.928	-0.103	0.042	0.055	040225.2	—
4-26	359.872	-0.073	0.056	0.048	020423.1	—
4-85	359.861	-0.091	0.058	0.053	030511.1	—
5-35	359.835	-0.115	0.070	0.079	030527.0	—
5-59	359.779	-0.118	0.048	0.050	030524.0	—
5-158	359.818	-0.090	0.085	0.083	020519.1	—
5-164	359.773	-0.115	0.046	0.047	020425.1	010311.2
6-17	359.884	0.043	0.035	0.034	020305.2	—

Table 3. (Continued)

6-21	0.017 -0.137	0.046	0.043	020221.4	—
6-23	359.980 -0.087	0.033	0.034	020311.2	—
6-28	359.960 -0.104	0.036	0.035	020220.3	—
6-31	359.974 -0.147	0.052	0.173	030524.0	—
6-32	359.957 -0.123	0.054	0.053	020221.2	—
6-57	359.979 -0.157	0.036	0.036	010309.2	020305.2
6-81	359.949 -0.125	0.046	0.041	030513.1	—
6-83	0.017 -0.102	0.039	0.036	020311.3	—
6-156	0.039 -0.129	0.055	0.047	020423.1	—
7-8	359.940 -0.139	0.061	0.056	030514.1	—
7-11	359.907 -0.179	0.050	0.046	020312.3	—
7-17	359.934 -0.153	0.043	0.041	020224.3	—
7-19	359.934 -0.170	0.053	0.048	020423.1	020423.1
7-31	359.894 -0.170	0.050	0.049	020219.3	—
7-86	359.935 -0.119	0.033	0.029	020312.2	020312.0
7-94	359.941 -0.167	0.049	0.046	030523.0	—
7-127	359.921 -0.200	0.061	0.064	020520.1	—
7-277	359.888 -0.147	0.038	0.043	020309.3	—
7-350	359.912 -0.122	0.076	0.080	020529.0	—
7-361	359.915 -0.169	0.031	0.029	020312.2	—
7-389	359.949 -0.127	0.054	0.050	030528.0	—
8-5	359.835 -0.241	0.049	0.179	030524.0	—
8-11	359.871 -0.171	0.034	0.036	010220.2	—
8-15	359.897 -0.214	0.067	0.069	030528.1	—
8-18	359.859 -0.220	0.051	0.045	010311.2	020220.4
8-97	359.874 -0.164	0.057	0.053	030511.1	—
8-264	359.873 -0.210	0.048	0.052	010309.3	020519.1
9-25	0.064 -0.063	0.054	0.052	030522.1	—
9-35	0.059 -0.090	0.051	0.053	020425.1	—
9-38	0.048 -0.086	0.038	0.034	020314.2	—
9-43	0.082 -0.050	0.049	0.044	030523.1	—
9-55	0.077 -0.044	0.047	0.045	020316.2	—
9-78	0.025 -0.055	0.042	0.039	020223.3	—
9-93	0.091 -0.085	0.043	0.039	020522.1	—
9-96	0.038 -0.107	0.044	0.040	020526.0	—
9-104	0.089 -0.053	0.040	0.039	020525.1	—
9-110	0.028 -0.096	0.036	0.035	020308.2	—

Table 3. (Continued)

9-124	0.090 -0.063	0.088	0.084	020521.1	—
9-229	0.040 -0.090	0.047	0.050	020529.0	—
10-1	0.120 -0.048	0.049	0.048	030514.0	—
10-4	0.163 -0.033	0.051	0.048	020530.1	—
10-55	0.121 -0.082	0.039	0.037	010221.3	020305.3
10-60	0.121 0.004	0.044	0.042	030510.1	—
10-66	0.132 -0.002	0.051	0.046	020530.1	010526.0
10-100	0.127 -0.004	0.050	0.050	020530.1	—
10-138	0.143 -0.037	0.168	0.154	020520.0	—
10-313	0.134 -0.023	0.066	0.064	020224.3	—
11-6	0.025 -0.186	0.044	0.044	010223.3	020528.1
11-14	359.999 -0.180	0.038	0.034	030529.0	020529.1
11-27	0.013 -0.213	0.050	0.053	020528.1	—
11-49	0.019 -0.157	0.053	0.243	030524.0	—
11-307	0.035 -0.181	0.042	0.046	040225.2	—
11-2449	0.060 -0.196	0.033	0.032	020526.1	—
12-2	0.084 -0.105	0.052	0.052	020521.0	—
12-11	0.137 -0.159	0.048	0.047	010520.0	020524.0
12-42	0.085 -0.122	0.054	0.341	030525.1	—
12-46	0.099 -0.098	0.067	0.067	020519.1	—
12-47	0.099 -0.107	0.047	0.045	030523.1	—
12-71	0.097 -0.103	0.044	0.040	030519.1	—
12-129	0.126 -0.136	0.046	0.044	020316.2	010309.3
12-136	0.104 -0.181	0.032	0.029	030517.1	—
12-140	0.058 -0.125	0.050	0.048	020524.0	—
13-4	0.159 -0.066	0.054	0.445	030526.1	—
13-6	0.179 -0.065	0.069	0.066	030528.1	—
13-13	0.190 -0.057	0.060	0.066	020523.0	010525.1
13-20	0.161 -0.074	0.055	0.049	030528.0	—
13-25	0.165 -0.096	0.049	0.054	010222.2	020224.2
13-30	0.159 -0.147	0.043	0.041	030519.1	—
13-33	0.180 -0.098	0.040	0.039	010308.2	—
13-44	0.198 -0.093	0.067	0.063	020224.3	—
13-45	0.138 -0.077	0.061	0.388	030526.0	—
13-49	0.160 -0.123	0.082	0.083	020521.1	—
13-64	0.180 -0.078	0.039	0.038	020316.3	—
13-73	0.159 -0.137	0.055	0.052	020424.2	—

Table 3. (Continued)

13-95	0.143 -0.104	0.046	0.040	030527.0	—
13-117	0.167 -0.105	0.161	0.166	020520.0	—
13-230	0.155 -0.070	0.034	0.035	020309.2	—
14-8	359.982 -0.201	0.054	0.051	020528.1	030527.0
14-12	359.947 -0.204	0.075	0.078	030527.0	—
14-15	359.933 -0.238	0.080	0.085	020519.1	—
14-16	359.959 -0.205	0.062	0.060	020224.4	—
14-17	359.962 -0.193	0.048	0.240	030525.1	—
14-24	359.956 -0.194	0.042	0.039	020525.0	010521.0
14-27	359.954 -0.246	0.052	0.046	020423.1	—
14-53	359.930 -0.199	0.058	0.359	030524.1	010522.0
14-105	359.987 -0.201	0.044	0.042	020529.1	—
14-150	359.991 -0.241	0.044	0.040	020224.3	—
14-463	359.945 -0.267	0.059	0.065	020523.0	—
14-6233	359.988 -0.179	0.052	0.231	030525.1	—
15-5	359.864 -0.247	0.055	0.054	020530.0	—
15-6	359.936 -0.257	0.053	0.052	020528.0	—
15-10	359.945 -0.275	0.044	0.044	020529.1	—
15-24	359.918 -0.232	0.052	0.052	020522.0	—
15-26	359.853 -0.255	0.058	0.380	030526.1	—
15-36	359.882 -0.250	0.050	0.049	010311.2	020521.1
15-47	359.904 -0.246	0.051	0.052	020530.0	—
15-81	359.911 -0.271	0.049	0.299	030524.0	—
16-32	359.902 0.020	0.054	0.050	020528.1	—
16-37	359.912 0.053	0.048	0.050	020529.0	—
16-59	359.936 0.004	0.035	0.034	020311.3	—
16-75	359.907 0.045	0.055	0.046	020423.1	—
16-93	359.882 0.002	0.050	0.053	020522.1	—
16-127	359.930 -0.007	0.053	0.053	030524.0	—
16-187	359.926 0.032	0.043	0.043	10520.0	—
16-227	359.874 0.042	0.054	0.052	030514.1	—
16-288	359.932 -0.001	0.049	0.116	030525.0	—
17-11	0.020 0.051	0.053	0.052	020530.0	—
17-15	0.008 0.055	0.045	0.045	020316.2	—
17-16	359.973 0.040	0.042	0.042	020223.3	—
17-57	359.967 0.040	0.040	0.043	030510.1	—
17-59	359.985 0.023	0.039	0.038	010404.2	020425.1

Table 3. (Continued)

17-70	359.982	0.046	0.038	0.040	020223.3	010223.4
17-119	359.976	0.063	0.062	0.064	020519.1	—
18-6	0.062	0.117	0.037	0.036	020316.2	—
18-12	0.059	0.082	0.036	0.037	020316.3	—
18-22	0.018	0.123	0.052	0.139	030526.1	—
19-3	359.823	-0.007	0.059	0.057	30524.1	—
19-45	359.872	-0.041	0.046	0.051	010521.0	020221.2
19-54	359.863	-0.008	0.042	0.041	030510.0	—
19-57	359.831	0.001	0.050	0.053	010522.1	020524.1
19-58	359.836	-0.004	0.046	0.043	020526.0	—
19-64	359.870	-0.045	0.050	0.045	030523.0	—
19-82	359.862	-0.035	0.035	0.036	020310.2	—
19-128	359.866	-0.021	0.036	0.039	020305.3	—
19-136	359.838	-0.052	0.054	0.049	030511.0	—
19-613	359.830	-0.070	0.050	0.048	020219.3	010519.0
19-660	359.822	-0.042	0.049	0.051	020530.0	—
19-3321	359.835	0.007	0.055	0.048	010521.0	020519.0
20-22	359.733	-0.040	0.046	0.046	020425.1	—
20-25	359.763	-0.032	0.047	0.046	010220.3	020521.1
20-34	359.754	-0.037	0.054	0.053	020530.0	—
20-38	359.763	-0.042	0.056	0.056	020224.4	—
20-43	359.773	-0.049	0.052	0.055	020522.0	—
20-46	359.746	-0.066	0.041	0.046	020220.2	010526.1
20-60	359.776	-0.054	0.033	0.033	020309.2	—
20-64	359.742	-0.031	0.050	0.051	020220.4	—
20-70	359.749	-0.055	0.058	0.108	030526.1	—
20-99	359.739	-0.053	0.050	0.047	020530.0	010520.1
20-133	359.762	-0.021	0.038	0.039	020525.0	—
20-522	359.790	-0.059	0.070	0.072	020521.1	—
21-38	359.686	0.012	0.044	0.044	020220.2	—
21-72	359.722	0.002	0.060	0.061	030526.1	—
21-185	359.745	0.038	0.032	0.032	020309.2	—
22-1	359.782	0.014	0.049	0.048	020219.3	010519.0
22-14	359.794	0.057	0.074	0.075	020529.0	—
22-16	359.789	0.014	0.031	0.029	020312.2	—
22-30	359.802	0.052	0.055	0.047	030511.0	—
22-31	359.793	0.012	0.049	0.044	030523.0	—

Table 3. (Continued)

22-60	359.808	0.086	0.058	0.051	010522.1	020519.0
22-85	359.837	0.025	0.063	0.056	030514.1	—
22-95	359.840	0.049	0.051	0.050	020221.2	—
22-100	359.750	0.050	0.053	0.050	010527.0	020522.0
22-136	359.781	0.042	0.054	0.056	010527.0	020224.4
23-15	359.843	0.080	0.047	0.045	030522.0	—
23-18	359.888	0.084	0.036	0.033	020311.3	—
23-28	359.868	0.088	0.050	0.051	010522.1	020519.1
23-30	359.865	0.069	0.058	0.059	010519.1	020220.3
23-32	359.864	0.045	0.036	0.034	020308.2	—
23-42	359.828	0.101	0.039	0.041	020424.1	—
23-46	359.873	0.053	0.040	0.042	020424.1	010519.0
23-50	359.816	0.102	0.040	0.043	030510.0	—
23-62	359.843	0.073	0.047	0.043	020526.0	—
23-75	359.845	0.082	0.050	0.052	020524.1	—
23-114	359.883	0.130	0.100	0.101	020219.3	—
23-3305	359.871	0.045	0.048	0.049	030525.0	—
23-371	359.890	0.073	0.041	0.040	020525.0	—
24-17	359.915	0.111	0.052	0.051	030522.1	—
24-28	359.932	0.093	0.057	0.054	030526.0	—
24-29	359.896	0.138	0.039	0.043	030510.1	—
25-7	359.975	0.201	0.052	0.051	030526.1	—
25-414	359.974	0.162	0.062	0.059	030526.0	—

‡ detected in Deguchi et al. (2000).

Table 4. Objects not listed in Tables 2 and 3, but regarded as observed

GMCS Name	Observed as	table	separation	comments
		listed	(")	
the same sources				
2-101	1-72	2	1.9	detected also on 20305.3
5-159	20-2631	2	0.7	detected also on 10527.1
9-75	12-46	3	2.1	nondetection
10-171	1-8	2	0.7	detected also on 20316.3
10-3465	13-18	2	0.4	detected also on 20524.0 at $V_{lsr} = 38 \text{ km s}^{-1}$; see text.
11-34	14-6233	3	3.6	nondetection
13-1856	12-51	2	2.4	detected also on 20525.1
14-32	7-52	2	0.6	detection
14-18	15-6	3	0.6	nondetection
16-80	3-271	3	2.7	nondetection
16-150	23-101	2	0.8	detected
16-24	17-1	2	2.8	detection
19-23	4-6	2	1.9	detected
21-8	20-22	3	1.7	nondetection
24-2	23-1198	2	0.8	detected
different sources				
2-19	2-504	2	10.5	nondetection
2-33	2-504	3	9.9	nondetection
3-162	3-49.2	2	10.7	detection, assignment impossible
3-1030	3-49.3	2	3.7	detection (=OH 359.906-0.036)
3-2753	3-72	2	4.9	detected but IRs10EE
3-2832	3-4969	2	5.3	detected component assigned to 3-4969 (OH source)
3-2834	17-1	2	11.6	detected component assigned to 17-1 (OH source)
6-7	6-57	3	8.6	nondetection
8-113	8-97	3	8.3	nondetection
9-3	9-110	3	11.4	nondetection
9-4	12-2	3	7.3	12-2 was not found in 2MASS
12-799	12-1236	2	6.5	detection, assignment impossible
16-2993	16-227	3	6.1	nondetection
17-58	17-8	3	3.5	detection, assignment impossible
22-5	22-21	2	10.5	double detections
22-120	22-31	3	5.4	nondetection

Table 5. Multiple detections and their assignment

Observed as	V_{lsr} (km s^{-1})	Assignment	separation ($''$)	comments
1-42.1*	43.8	assignment impossible		1-182(17.8''; negative)
1-42.2	57.3	assignment impossible		
2-11.1	-23.0	2-11	0.0	
2-11.2	-6.6	\sim OH359.998-0.005	19.5	this is not 2-10
2-26.1	-63.9	assignment impossible		2-11 (26.2''; -23 kms^{-1})
2-26.2*	151.6	assignment impossible		and 2-46 (32.8''; negative), both seem not
3-5.1	35.8	\sim 3-16	16.7	$V_{lsr} = 32.8$
3-5.2	52.8	3-5	0.0	=OH359.956-0.050
3-49.1	-140.9	\sim 3-779		=OH359.906-0.041(-140.8 kms^{-1})
3-49.2	-98.7	assignment impossible		3-162 close (10.4'')
3-49.3	-48.7	\sim 3-1030	3.7	=OH359.906-0.036 (-46.8 km s^{-1})
3-88.1	-114.8	assignment impossible		close to 3-270 (19.8''; negative)
3-88.2*	8.4	assignment impossible		but this is negative
3-779.1	-141.7	3-779	0.0	=OH359.906-0.041
3-779.2	-47.6	\sim 3-1030		=OH359.906-0.036
5-157.1	-2.3	assignment impossible		
5-157.2*	6.8	assignment impossible		
9-8.1	-4.4	9-8	0.0	
9-8.2	72.5	\sim 9-547	14.5	=OH0.040-0.056
9-547.1	-3.9	\sim 9-8	14.5	
9-547.2	72.5	9-547	0.0	=OH0.040-0.056
12-21.1	33.2	(or 12-42)	(24.8)	assignment difficult
12-22.2	71.4	\sim 12-65	20.7	assignment difficult
16-1.1	-5.1	\sim OH359.867+0.030	9.8	
16-1.2	22.1	16-1	0.0	
16-77.1	-28.2	assignment impossible		16-127 (18.4'';negative)
16-77.2*	244.2	assignment impossible		16-29 (26.9'';46.9 kms^{-1})
18-190.1	-48.0	assignment impossible		no closeby source
18-190.2*	101.6	assignment impossible		
19-7.1	-105.6	19-7	0.0	
19-7.2	-31.9	\sim 19-9	15.9	
19-685.1	-53.4	assignment impossible		19-128(16.3'';negative)
19-685.2	-44.2	19-685	0.0	=OH359.868-0.018
22-21.1	12.1	assignment impossible		close to 22-5(10.0'')

Table 5. (Continued)

22-21.2*	156.2	assignment impossible		
22-21.3	165.6	assignment impossible		
23-10.1	-299.4	23-10	0.0	=OH359.779+0.010
23-10.2	-139.8	23-7	12.9	23-7 detected

* indication that the star is tentatively assigned to the stronger SiO source for convenience.

Table 6. Comparison with OH observations

Observed as	V_{lsr}^{SiO}	OH Name	V_{lsr}^{OH}	separation	comments
	(km s ⁻¹)	listed	(km s ⁻¹)	(")	
1-1890	23.6	0.083+0.063 \ddagger	24.8	1.7	
2-10 †	-6.9	359.998-0.005	-6	15.8	this is not 2-10
2-11.2†	-6.6	359.998-0.005	-6	19.5	this is not 2-10
2-28	36.0	0.037-0.003	34.9	2.9	
2-320	-4.7	0.060-0.018	-4.3	1.7	
2-504	—	0.030-0.026	-55.1	1.7	
2-697	-53.2	0.024+0.027	-50.7	1.8	
2-6329	114.7	0.014-0.046	117.8	1.4	
3-3	—	359.970-0.049	88.8	2.1	
3-5.2	52.8	359.956-0.050	48.5	2.0	
3-101†	24.0	359.965-0.043	-55.3	2.6	3-6 (17.0"; 23.0 km s ⁻¹)
3-205†	-93.6	359.932-0.059	-151.7	1.4	this is OH359.931-0.063 (12.5"; -93.7 km s ⁻¹)
3-226	134.2	359.946-0.092	132.3	1.2	
3-266	-73.0	359.937-0.010	-73.0	1.7	
3-358	12.9	359.985-0.061	13.3	2.3	
3-779	-141.7	359.906-0.041	-140.8	0.1	
3-885	65.9	359.954-0.031	66.1	1.2	
3-1030 (3-779.2)	-48.7	359.906-0.036	-46.8	1.8	also observed as 3-49.3
3-2389	54.0	359.938-0.052 \flat	53.1	1.8	
3-2752	5.7	359.985-0.042	2.0	2.7	
3-2855	-308.1	359.918-0.055	-307.9	1.0	
3-4969	108.6	359.999-0.061	106.4	2.4	
4-113†	-289.4	359.855-0.078 \ddagger	5.2	0.3	inconsistent
4-340	-55.3	359.888-0.051	-57.3	2.9	
4-557	-85.1	359.902-0.103	-85.6	1.4	
5-10.2	-31.0	359.814-0.162	-31.1	0.8	
5-2856	71.0	359.776-0.120	72.3	2.4	
6-21	—	0.017-0.137	108.3	2.0	
6-32	—	359.957-0.123	-157.5	1.1	
6-135	5.8	0.007-0.089 \ddagger	3.7	0.6	
8-264	—	359.872-0.210	12.4	0.7	
9-49	-14.0	0.053-0.063	-11.5	0.9	
9-547.2	72.5	0.040-0.056 \flat	71.8	2.9	also observed as 9-8.1
10-6	39.5	0.107-0.016	40.8	1.3	

Table 6. (Continued)

10-84	-27.9	0.115-0.043	-29.7	0.7	
10-313	—	0.134-0.023	-20.2	1.0	
10-392	94.3	0.128-0.020	94.5	0.9	
11-4503	7.9	0.015-0.171	8.1	1.8	
12-51	44.3	0.138-0.136	40.1	2.4	
12-145	34.5	0.067-0.123	35.7	0.9	
13-33	—	0.180-0.098	120.7	0.4	
13-200	23.7	0.178-0.055	-36.6	5.1	different source
13-1856	—	0.138-0.136	40.1	0.4	
16-1.1†	-5.1	359.867+0.030	-3.7	9.6	not 16-1
16-49	-72.	359.938-0.010	-73.3	2.0	
16-187	—	359.925+0.032	-83.2	2.9	
17-630	-9.8	359.947+0.066	-9.4	2.0	
17-3762	-49.0	359.990+0.030	-50.2	2.4	
18-74	121.3	0.051+0.079	117.0	0.4	
18-173	73.9	0.042+0.082	74.2	1.0	
19-476	-74.9	359.797-0.025	-71.2	3.4	
19-582	-50.2	359.825-0.024	-53.6	2.9	
19-613	—	359.830-0.070	-82.7	0.3	
19-685	-44.2	359.868-0.018	-43.4	2.8	
20-26	-38.4	359.810-0.070‡	-36.9	1.3	
20-38	—	359.763-0.042‡	120.7	0.4	
20-136	-95.4	359.791-0.081	-116.8§	0.7	OH single peak detection
20-2631	-4.0	359.799-0.090	-4.3	1.3	
22-4	-68.6	359.837+0.052	-69.0	2.9	
22-76	-77.3	359.837+0.030	75.2	2.7	
22-274†	-81.2	359.779+0.010	-27.5	0.6	inconsistent (22-34? 31.4")
23-10.1	-299.4	359.864+0.056	-300.6	0.6	
23-30	—	359.864+0.068	66.1	2.2	
23-101(=6-150)	-132.0	359.902+0.061	-133.6	0.4	
25-234	104.9	0.018+0.156	103.0	0.6	
25-414	—	359.974-0.058	26.0	0.5	

† contamination.

§ OH single peak.

‡ SiO also detected by Sjouwerman et al. (2002).

§ see figure 11 of Sjouwerman et al. (1998).

fig2a.eps

fig2b.eps

fig2c.eps

fig2d.eps

fig2e.eps

fig2f.eps

fig2g.eps

fig2h.eps

fig2i.eps

fig2j.eps

fig2k.eps

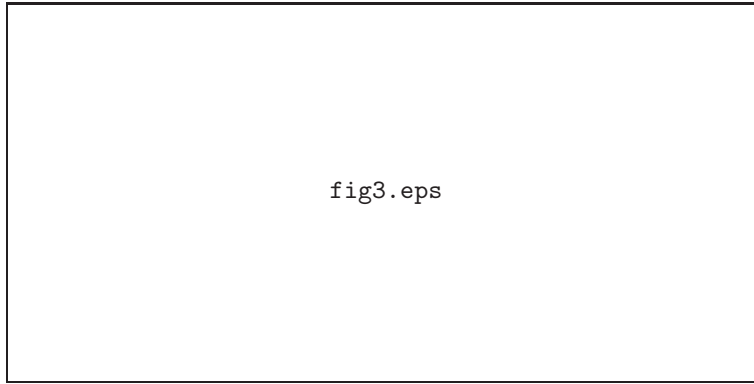


Fig. 3. Histogram of period and detection probability (line graph). The shaded and unshaded area of the histogram indicate the SiO detection and nondetection, respectively. The line graphs with filled and unfilled circles indicate the detection rate of SiO and OH masers, respectively, for the observed sources (unit at the right vertical axis).

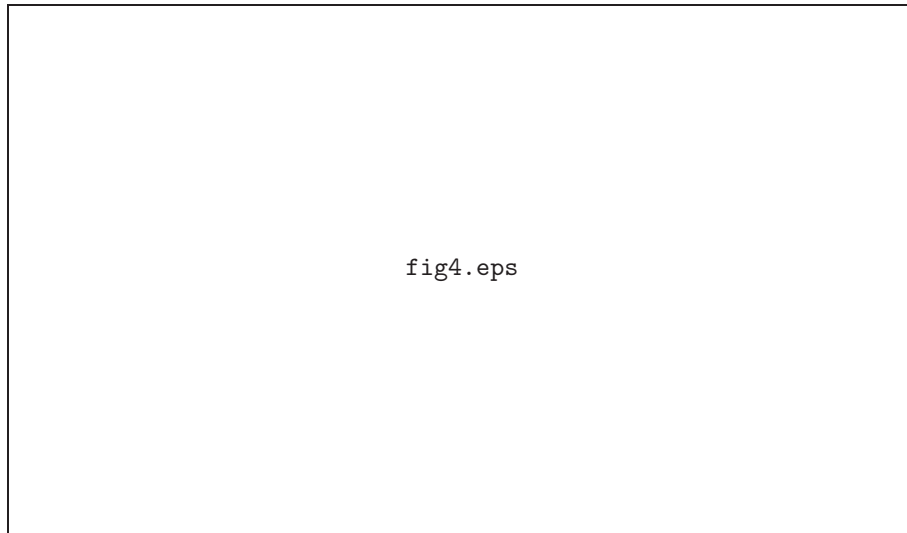


Fig. 4. Normalized accumulation number with respect to r^2 for all the LAVs and SiO detections (left panel), that for SiO detections at $l^* > 0$ and at $l^* < 0$ (center panel), and that for OH sources in a OH survey, and LAV with OH, and LAV with SiO in the present sample (right panel). The OH surface-density distribution in the OH survey ($N \sim r^{0.8}$) is apparently different from the distribution of the LAVs with SiO (and that of LAVs; $N \sim r^{1.3}$). The horizontal axis is taken as r^2 , so that the constant surface density gives a straight line ($N \sim r^2$) in this figure.

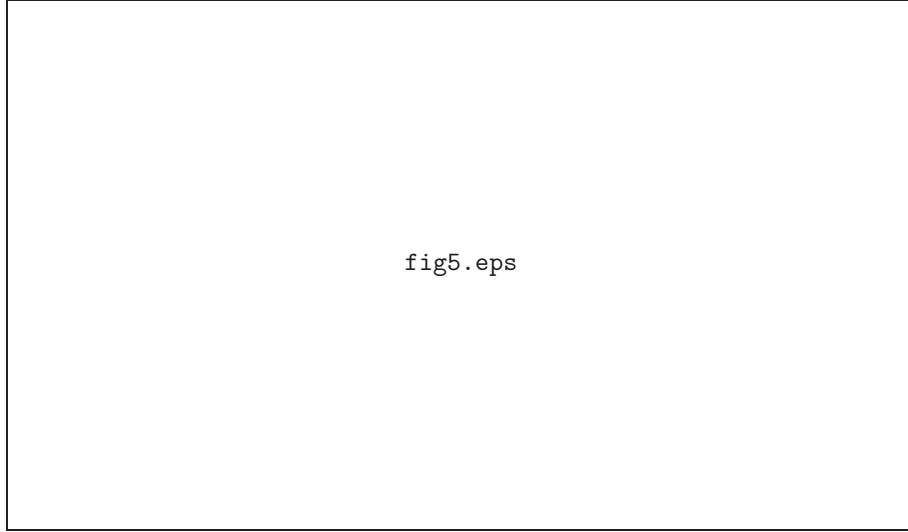


Fig. 5. Longitude-Velocity diagram of the SiO detections. Filled circles indicate the objects with $r < 5'$ on the left panel and with $r < 3'$ on the right panel. The regression lines are indicated by broken or solid lines for each sets. The CO (left panel) and CS (right panel) $J = 1-0$ $l-v$ diagram at $b \sim -4'$ (Oka et al. 1998; Tsuboi et al. 1999) are overlaid.



Fig. 6. Mass distribution in the galactic center area. Filled triangles and diamonds indicate the enclosed masses obtained for SiO maser data set by the pressure-balance (PB) and projected-mass (PM) methods, respectively. Open triangles and diamonds indicate the mass from the OH-maser data set (Lindqvist et al. 1992) with the same two methods. The thick and thin curves with filled squares and circles indicate the mass obtained by the present method for rotational and non-rotational cases, respectively. statistical errors are also shown by tickmarks.

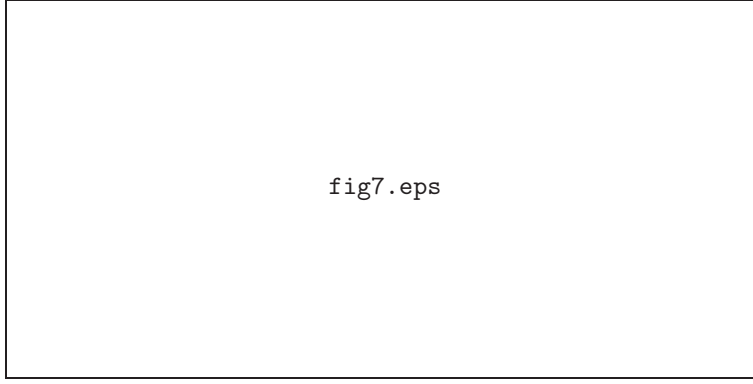


Fig. 7. Plot of projected mass versus projected distance. Circles indicate the projected mass for individual object. The dotted and broken curves indicate $q = 2G^{-1}R[U(R_0) - U(R)]$, where R_0 is indicated. Thick solid curve with sign " M_R " indicate the calculated enclosed mass. Note that these circles and curves are plotted with r and R , respectively, but are plotted using the same axis in this figure. Because of inequalities (12) and (13), the projected quantities, (r, q) , give the lower bound for $(R, 2G^{-1}R[U(R_0) - U(R)])$ for the particular object. Several extremely high velocity object are located out of this diagram and are not shown.



Fig. 8. K Magnitude–Period diagram for SiO detected objects. Open circles indicate the stars with $q > 2G^{-1}r[U(30pc) - U(r)]$ and $V_{lsr} > 0$, filled circles the stars with $q > 2G^{-1}r[U(30pc) - U(r)]$ and $V_{lsr} < 0$, and the crosses the stars with $q < 2G^{-1}r[U(30pc) - U(r)]$.

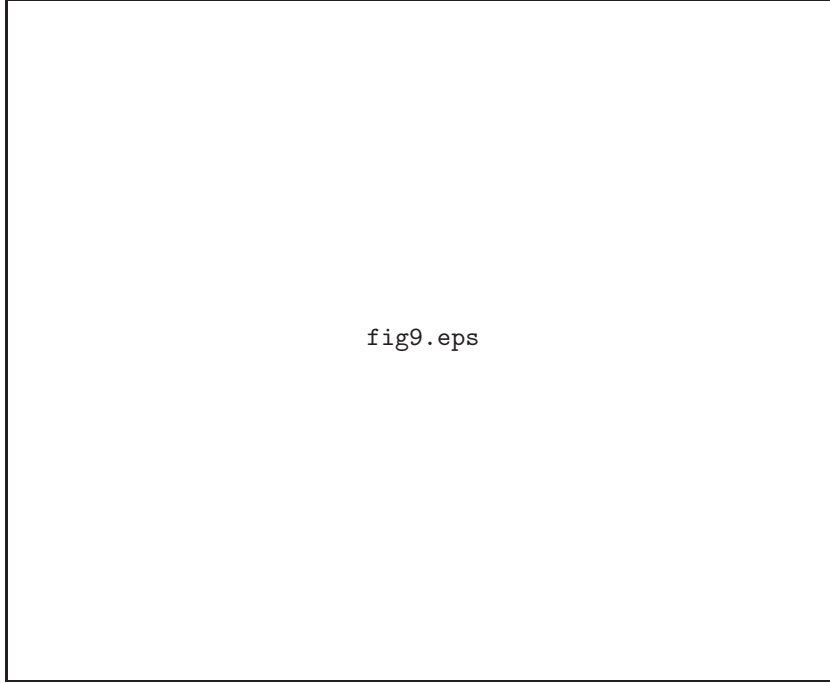


Fig. 9. Cylindrical coordinates and relations of the rotational vectors. The observer is located at the infinitely distant point on the z-axis. It is assumed that the system rotates around y-axis, and that the rotational velocity, V , decreases with the cosine law [proportional to $(x^2 + z^2)^{0.5}/R$]. Using $V_{\text{rot},r} = V_x \cos(\phi)$ and $V_{\text{rot},\phi} = -V_x \sin(\phi)$, and $x = r \cos(\phi)$ and $y = r \sin(\phi)$, we obtain equations (24)–(26).

This figure "fig1.jpg" is available in "jpg" format from:

<http://arxiv.org/ps/astro-ph/0403113v1>

This figure "fig2a.jpg" is available in "jpg" format from:

<http://arxiv.org/ps/astro-ph/0403113v1>

This figure "fig3.jpg" is available in "jpg" format from:

<http://arxiv.org/ps/astro-ph/0403113v1>

This figure "fig4.jpg" is available in "jpg" format from:

<http://arxiv.org/ps/astro-ph/0403113v1>

This figure "fig5.jpg" is available in "jpg" format from:

<http://arxiv.org/ps/astro-ph/0403113v1>

This figure "fig6.jpg" is available in "jpg" format from:

<http://arxiv.org/ps/astro-ph/0403113v1>

This figure "fig7.jpg" is available in "jpg" format from:

<http://arxiv.org/ps/astro-ph/0403113v1>

This figure "fig8.jpg" is available in "jpg" format from:

<http://arxiv.org/ps/astro-ph/0403113v1>

This figure "fig9.jpg" is available in "jpg" format from:

<http://arxiv.org/ps/astro-ph/0403113v1>